Computers and Geotechnics 173 (2024) 106517

Contents lists available at ScienceDirect

Computers and Geotechnics

journal homepage: www.elsevier.com/locate/compgeo

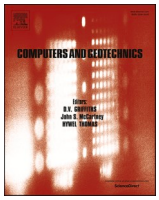

Research Paper

A 2D continuous-discontinuous unified pore-fracture seepage model for hydro-mechanical coupling in the combined finite-discrete element method (FDEM) using node binding scheme

Weibing Cai [a], Ke Gao [a,b,*], Yan Qiao [c], Shu-Gang Ai [a], Yu Feng [d]

[a] Department of Earth and Space Sciences, Southern University of Science and Technology, Shenzhen, Guangdong, China
[b] Guangdong Provincial Key Laboratory of Geophysical High-resolution Imaging Technology, Southern University of Science and Technology, Shenzhen, Guangdong, China
[c] CNPC Engineering Technology R&D Company Limited, Beijing, China
[d] School of Civil Engineering, Sun Yat-sen University, Zhuhai 519082, China

ARTICLE INFO

Keywords:
Combined finite-discrete element method (FDEM)
Node binding scheme
Pore seepage
Fracture seepage
Fluid-driven fracture
Hydraulic fracturing

ABSTRACT

The combined finite-discrete element method (FDEM) has been widely used to simulate the dynamic propagation of hydraulic fractures. In the conventional FDEM, a fictitious fluid exchange coefficient between adjacent finite element pairs needs to be specified to alleviate the discontinuous pore seepage in the continuous rock matrix domain. This commonly employed approach inevitably increases computational cost and introduces additional numerical parameters (e.g., fluid exchange coefficient). To circumvent these limitations, we propose a node binding scheme that not only ensures continuous pore seepage simulations in the intact/continuous rock matrix domain, but also allows discontinuous pore pressures on the two sides of a fracture. The computational efficiency of pore seepage simulation using the proposed approach is increased by ~120 times for a model with ~6000 triangle elements, and fictitious numerical parameters are not required. A suite of numerical benchmarks is conducted to verify the effectiveness and robustness of the proposed pore-fracture seepage model, and its capability of capturing the dynamic propagation process of fluid-driven fractures is also demonstrated. As an application, a typical example is employed to explore the mechanism of multiple hydraulic fracturing. The proposed hydro-mechanical coupling model may help enhance the applicability and accuracy of FDEM for unconventional energy exploitation.

1. Introduction

Rock masses comprise intact porous matrices and embedded fractures. Thus, fluid flow in rock masses mainly involves two aspects, i.e., pore seepage and fracture seepage. In the processes of many rock engineering applications (e.g., unconventional energy exploitation, deep underground disposal of nuclear waste, and underground storage of oil and gas), accurate evaluation of pore seepage and fracture seepage in fractured porous rock media plays a significant role in uncovering the underlying mechanisms of fluid-driven fractures and providing insights into the complex interplay between fluid flow and rock masses behavior (Nagel et al., 2013). Therefore, establishing a robust model that can simultaneously consider pore seepage and fracture seepage is crucial for the optimal design and safety of various rock engineering applications (Berkowitz, 2002).

Numerical simulations are considered as an essential complement to analytical and experimental methods, and have been extensively employed in recent years to investigate hydraulic fracturing mechanisms in fractured porous media (Qin et al., 2021; Sun et al., 2022; Ulloa et al., 2022; Yu et al., 2021). In general, seepage models in numerical simulations can be established using continuum-based or discontinuum-based approaches (Jing and Hudson, 2002). Continuum-based approaches, such as the finite element method (FEM) (Lewis and Schrefler, 1998), boundary element method (BEM) (van Opstal and van Brummelen, 2013) and finite volume method (FVM) (Mosharaf-Dehkordi, 2022), can effectively simulate poroelastic problems using Biot's theory by treating both rock matrices and fractures as homogeneous porous media. Then, the dual-porosity model is employed to simulate fracture seepage in discontinuous porous media, where the pore pressure on the two sides of a fracture is continuous due to the same node shared by the

* Corresponding author at: Department of Earth and Space Sciences, Southern University of Science and Technology, Shenzhen, Guangdong, China.
E-mail address: gaok@sustech.edu.cn (K. Gao).

https://doi.org/10.1016/j.compgeo.2024.106517
Received 3 January 2024; Received in revised form 24 May 2024; Accepted 5 June 2024

matrices on the two sides of a fracture (Barenblatt et al., 1960). Recently, the discrete fracture matrix (DFM) model has also been introduced to deal with fractured rock masses with a limited number of fractures (Gläser et al., 2017). However, this model assumes that fluid flows only occur in the fracture network and thus fail to couple the pore pressure in continuous rock domains.

To consider the strain localization and fracturing of rock masses, advanced numerical methodologies based on continuous framework have been proposed in the literature, such as meshfree methods (Belytschko et al., 1994), generalized finite element method (GFEM) (Duarte et al., 2001), extended finite element method (XFEM) (Khoei et al., 2018; Lamb et al., 2013) and phase field (PF) (Xing and Zhao, 2023). Among them, although XFEM overcomes the dynamic mesh regeneration induced by crack propagation, it may lead to significant computational costs due to the requirement of refined mesh. Moreover, this method fails to effectively deal with the interaction of crack surfaces for closing cracks. The advantages of PF lie in its capability to simulate crack initiation, propagation, and coalescence driven by fluid seepage. However, cracking healing and fracture aperture evolution cannot be well captured in PF.

The discontinuum-based discrete element method (DEM) has also found broad applications in brittle rock-related simulations, in which the rock matrix is simulated as rigid particles or blocks bonded by spring with normal and tangential stiffness (Cundall and Strack, 1979). For example, in the PFC (Particle Flow Code) software developed based on DEM, the pipe-network modeling algorithm is adopted to capture fluid seepage by establishing a two-layer topological structure formed by the pipe domains (Cai et al., 2022). In PFC, the pore seepage of rock matrix is approximately implemented by fluid flow along the initial fracture aperture between adjacent domains using cubic law. Compared to fracture seepage, fracture aperture associated with pore seepage remains unchanged, thereby leading to the dependence of the permeability of rock matrix on the initial fracture aperture. Consequently, this model fails to simulate pore and fracture seepage simultaneously and accurately when the permeability of fracture is much higher than that of rock matrix. In addition, it is challenging to establish a clear relationship between the rock matrix permeability and initial fracture aperture in PFC (Duan et al., 2021). Similar criticisms have been made for many other discontinuum-based numerical methods, such as UDEC (Universal Distinct Element Code) (Board, 1989) and DDA (Discontinuous Deformation Analysis) (Shi and Goodman, 1985).

Due to the complex continuum-discontinuum characteristics of fractured rock masses, the combined finite-discrete element method (FDEM), proposed by Munjiza (1992), has recently been used to simulate the progressive fracturing behavior of brittle materials (Euser et al., 2019; Wu et al., 2021). FDEM combines the advantages of FEM and DEM, and thus provides a promising solution to simulate the fracturing process from continuum to discontinuum. In particular, large displacement sliding, shearing and discrete block movement can be effectively captured and evaluated with the energy-conserving contact model. Within the framework of FDEM, Yan and Zheng (2016) propose a coupled hydro-mechanical model to simulate hydraulic fracturing, where both pore seepage and fracture seepage are considered. In the meantime, the same hydro-mechanical model based on GPGPU parallelization was incorporated into the commercial FDEM software – Irazu (Lisjak et al., 2017). However, similar to PFC, the implementation of the real pore seepage in rock matrices in these applications is still not satisfactory due to the high dependence of rock permeability on the initial fracture aperture. To circumvent this limitation, Yan and Jiao (2018) proposed a 2D fully coupled model that incorporates both real pore seepage and fracture seepage. In their model, the fracture flow is controlled by the cubic law, and the pore seepage in rock matrices is characterized by Darcy's law using the FVM, which alleviates the dependence of rock matrix permeability on the initial fracture aperture.

However, the current hydro-mechanical model in FDEM with intrinsic cohesive model still has two drawbacks that may need further improvement. First, because the node number of porous matrices does not experience splitting when a new fracture occurs, the pore pressures at the two sides of the newly generated fracture are inappropriately identical. Second, a fluid exchange coefficient of cohesive element is required to approximate the continuity of pore seepage in rock matrices, which introduces an additional numerical parameter (i.e., the fluid exchange coefficient) and also increases the computing overhead. For the first problem, a mixed fracture-pore seepage model in fractured porous media is presented by Yan et al. (2021), where two sets of node networks are employed to achieve the discontinuity of pore pressure on the two sides of a fracture. Nevertheless, the appropriate selection of the fluid flux exchange coefficient between the fracture and rock matrix brings a new challenge because the same fluid flux exchange would elicit different fluid pressure responses in the two seepage models. This challenge highlights the need for careful consideration and calibration of the exchange coefficient to ensure the accuracy and reliability of the hydro-mechanical coupling model. Recently, efforts have been made to circumvent the second problem by dynamically updating the node sharing connections between neighboring elements in the framework of FDEM (Yan et al., 2022a; Yan et al., 2023). However, details of the approach have not been made readily available in the existing literature, rendering its practical implementation and effectiveness unclear.

In this work, based on our 2D in-house FDEM code – Pamuco, we introduce a novel node binding scheme to establish a continuous-discontinuous unified pore-fracture seepage model for hydro-mechanical coupling. The model not only ensures the continuity of pore seepage simulations in the intact/continuous deformation domain prior to fracturing onset, but also significantly reduces the computational cost of the pore seepage module. Additionally, the proposed model considers the discontinuous pore pressures on the two sides of a fracture, thereby achieving the pore pressure discontinuity across fractures. The fracture seepage model based on cubic law is adopted to simulate fluid flow along fractures. It must be noted that in saturated or unsaturated porous media, the fluid pressure is not necessarily discontinuous at the sides of the fracture. On the contrary, continuous fluid pressure but discontinuous pressure gradient (i.e., the weak discontinuity) is a more reasonable assumption in most cases when the width of the fracture is very small compared to other dimensions of the medium (Khoei and Mortazavi, 2020; Mohammadnejad and Khoei, 2013; Ni et al., 2021; Réthoré et al., 2007; Schwartzkopff et al., 2021; Vahab et al., 2019). However, if the numerical model contains large fracture networks with various fracture apertures, our proposed model can also achieve discontinuity across the two sides of the fracture.

The remainder of this paper is organized as follows. The fundamental principles of FDEM are briefly introduced in Section 2. In Section 3, the unified pore-fracture seepage model is proposed in the current framework of FDEM. In Section 4, a series of benchmark cases are performed to verify the accuracy and robustness of the proposed hydro-mechanical coupling model, and its advantage in terms of computational efficiency is also presented. Following this, an application case is provided to demonstrate the potential of the proposed approach in elucidating the mechanisms of multiple hydraulic fracturing in Section 5. Conclusions are drawn in Section 6.

2. Fundamentals of FDEM

In this section, we first introduce the nodal motion equation and the rock fracturing model used in FDEM. Then, the contact detection and interaction algorithm are briefly discussed.

2.1. Motion equation

In 2D FDEM models, the solid matrix is discretized into an assembly of three-node triangle finite elements, and explicit time integration schemes are adopted to solve the nodal motion equations, which can be written as (Munjiza, 2004)

$$\mathbf{M}\ddot{\mathbf{u}} + \mathbf{C}\dot{\mathbf{u}} = \mathbf{f} \tag{1}$$

where **M** is the mass lumping matrix, **C** is the damping matrix, **u** is the nodal displacement vector, $\ddot{\mathbf{u}}$ and $\dot{\mathbf{u}}$ are respectively the nodal acceleration and velocity vectors, and **f** represents the total force vector. The damping matrix is introduced to consume kinetic energy for quasi-static equilibrium cases (i.e., the so-called dynamic relaxation).

2.2. Rock fracturing modeling

Rock failure is a progressive damage process where microcracks are first initiated from fracture tips and gradually develop into meso- or macro-fractures. To simulate fracture initiation and propagation in rock masses, four-node cohesive elements with zero initial thickness are inserted between adjacent triangle finite elements before the onset of simulation to capture the fracture process zone (FPZ). The cohesive tractions of each cohesive element, i.e., σ^{coh} and τ^{coh} between the common edges of a triangle finite element pair, is denoted as a function of the relative displacements of the two edges of the cohesive element, i.e., o and $|s|$, in the normal and tangential directions, respectively (see Fig. 1). At present, the fracturing modes of cohesive elements mainly consist of three types, i.e., Mode I (tensile fracturing), Mode II (shear fracturing), and mixed Mode I-II (tensile-shear mixed fracturing). As shown in Fig. 1a, when the normal opening o increases to the elastic limits o_p, the normal cohesive stress (σ^{coh}, tensile positive) reaches the tensile strength f_t, which marks the damage initiation point of a cohesive element. As o continues to increase, the cohesive element starts to damage. When o reaches the critical (maximum) normal opening o_t, i.e., the breakage point of cohesive element, a pure tensile microcrack will be generated (Mode I). Similarly, as presented in Fig. 1b, the shear cohesive stress (τ^{coh}) reaches the shear strength f_s when the tangential slipping $|s|$ increases to the elastic limits s_p. Specifically, the peak shear strength is defined using the Mohr-Coulomb criterion as

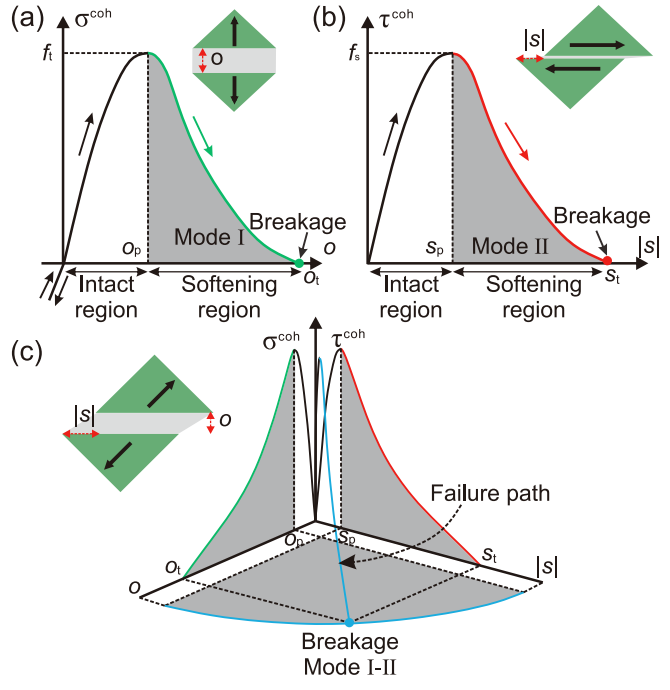

Fig. 1. Constitutive laws of cohesive elements. (a) Constitutive of tensile fracturing mode, i.e., Mode I. (b) Constitutive of shear fracturing mode, i.e., Mode II. (c) Constitutive of mixed fracturing mode, i.e., mixed Mode I-II. Here, o and $|s|$ represent the relative opening and slipping displacement of a cohesive element, respectively; o_p and s_p are the elastic limits of o and $|s|$, respectively; o_t and s_t are the critical values of o and $|s|$, respectively; f_t and f_s are the tensile and shear strength of cohesive element, respectively.

$$f_s = \begin{cases} c & \text{if } \sigma^{coh} \geqslant 0 \\ c - \sigma^{coh}\tan\varphi & \text{if } \sigma^{coh} < 0 \end{cases} \tag{2}$$

where c and φ are the cohesion and internal friction angle of the cohesive elements, respectively. The cohesive element breakage of the mixed Mode I-II is determined by the combined effect of normal opening and tangential slipping (Fig. 1c). Note that the mixed Mode I-II includes two fracturing scenarios, i.e., tensile-shear fracturing and compressive-shear fracturing. More details on the constitutive laws of cohesive elements can refer to previous works (Fukuda et al., 2019b; Han et al., 2020; Tatone and Grasselli, 2015).

2.3. Contact model

The contact algorithm for processing the interaction between neighboring finite elements in FDEM involves contact detection and contact interaction. The contact detection is to determine contact couples of finite elements in touch. The efficient NBS (non-binary search) algorithm is commonly used in FDEM for contact detection, which yields a theoretical CPU time proportional to the total number of finite elements (Munjiza and Andrews, 1998). After obtaining the contact couples, the contact interaction algorithm is invoked to calculate the contact forces. More details on contact detection and interaction are available from previous publications (Munjiza, 2004; Munjiza et al., 2011).

3. Proposed pore-fracture seepage model

3.1. Governing equations of seepage models

The pore seepage describes the porous flow in rock masses, and its governing equation integrates mass conversation with Darcy's law and is given as (Lobao, 2007; Yan et al., 2022b):

$$\frac{1}{M_b}\frac{\partial p^p}{\partial t} = -\frac{\partial q_i}{\partial x_i} - \alpha\frac{\partial \varepsilon_v}{\partial t} \tag{3}$$

where p^p is the pore pressure of the solid matrix, α is the Biot coefficient, M_b is the Biot modulus ($M_b = K_w/\psi$, K_w is the bulk modulus of fluid, ψ is porosity), and ε_v is the mechanical volumetric strains of the solid matrix. For the fracture seepage model, it is assumed that the fracturing fluid is incompressible, laminar with a low Reynolds number, and locally similar to the parallel-plate flow. The governing equation of fracture seepage using the cubic law is (Profit et al., 2016; Yan et al., 2022b)

$$\frac{\partial p^f}{\partial t} = K_w\left(-\frac{\partial q_i}{\partial x_i} - \frac{\partial \varepsilon_f}{\partial t}\right) \tag{4}$$

where p^f is the fracture pressure, and ε_f is the volumetric strain of the fracture.

3.2. Pore seepage model

To ensure the continuum behavior of pore seepage in intact porous media and to improve computational efficiency, we borrow a strategy from the node binding scheme initially proposed in our previous work to avoid redundant fluid exchange between adjacent finite element pairs in the elastic domain due to the existence of cohesive elements (Cai et al., 2023; Fukuda et al., 2020; Maeda et al., 2024). As shown in Fig. 2, the porous medium is meshed into ten triangle elements before the simulation starts; these triangle elements are then discretized into independent ones (without node sharing), and adjacent finite elements are rejoined with four-node zero-initial-thickness cohesive elements. We preserve the mapping information from the original nodes before model discretization (denoted as master nodes, e.g., Nodes m_1 and m_2 in

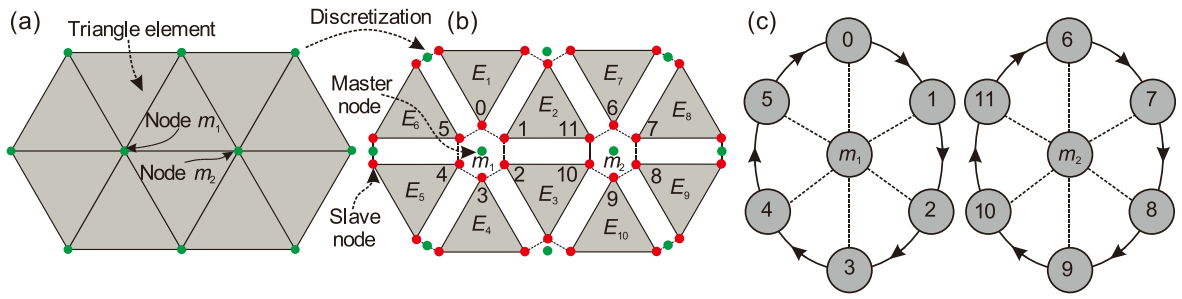

Fig. 2. Mesh discretization and re-joining of triangle finite elements using cohesive elements. Nodes 0 to 5 are slave nodes bound together as a group identified by a master Node m_1; similarly, slave Nodes 6 to 11 are bound together and identified by master Node m_2.

Fig. 2a) to the corresponding new nodes after model discretization (denoted as slave nodes, e.g., Nodes 0 to 11 in Fig. 2b) in a master–slave manner. Each master node corresponds to several slave nodes, forming a master–slave group. This mapping information between the master and slave nodes can be saved in a list such as $0 \rightarrow m_1$, $1 \rightarrow m_1$, …, $5 \rightarrow m_1$ and $6 \rightarrow m_2$, $7 \rightarrow m_2$, …, $11 \rightarrow m_2$ (Fig. 2c). If a master node is located inside the model (i.e.., no connection to any boundaries, e.g., Node m_1 and m_2), all its slave nodes will be stored in a circular linked list according to their relative positions, e.g., $0 \rightarrow 1 \rightarrow 2 \rightarrow 3 \rightarrow 4 \rightarrow 5 \rightarrow 0$ (corresponding to master Node m_1), and $6 \rightarrow 7 \rightarrow 8 \rightarrow 9 \rightarrow 10 \rightarrow 11 \rightarrow 6$ (corresponding to master Node m_2) (Fig. 2c).

It is worth noting that the master nodes from the original mesh are merely used as identifiers for each slave node group. To avoid fluid exchange through cohesive elements between adjacent finite elements during the elastic deformation stage, we bind the slave nodes in each group. The fluid flow rate and nodal masses of slave nodes in each group are all accumulated to their master node. At the end of each iteration, the updated fluid pressure of all slave nodes in the same group needs to be synchronized as the same as their master node. In other words, the slave nodes in the same group will share identical information (i.e., fluid flux and pore pressure) with their master node in the intact/continuous deformation domain. Therefore, only pore seepage in triangle elements is calculated according to Darcy's law, which is more reasonable and accurate and can also reduce the computational cost (as will be demonstrated in Section 4.5).

Note that in our previous work (Cai et al., 2023), we propose a node binding scheme to simulate rock fracturing using the extrinsic cohesive zone model. However, the "time discontinuity" problem pointed out in previous studies is not well-addressed (Fukuda et al., 2021; Knight et al., 2020; Papoulia et al., 2003; Sam et al., 2005), where the discontinuity of local nodal forces occurs before and after the insertion of a cohesive element due to the inconsistent constitutive models used for finite elements and cohesive elements in terms of nodal force calculation. When hydraulic fracture propagates, an accurate assessment of fracture aperture is crucial for the fracture seepage model. Unfortunately, the unsolved "time discontinuity" may obtain inaccurate fracture aperture, thereby leading to spurious simulated results of fracture seepage. Therefore, only the pore seepage rather than the cohesive zone model adopts the node binding scheme in this study.

For each triangle element, the flow rate of the master node along the i^{th} direction ($i = 1, 2$, corresponding to x and y direction), q_i, is described by

$$q_i = -\rho_f g \frac{k_{ij}}{\mu_f} \frac{\partial h}{\partial x_j} \quad (i,j = 1,2) \tag{5}$$

Here, ρ_f is the fluid density, g is the acceleration of gravity, k_{ij} is the intrinsic permeability, μ_f is the fluid viscosity, and h is the total head of the master node, i.e.,

$$h = (P - \rho_f g y)/(\rho_f g) \tag{6}$$

where P is the pore pressure of the master node, and y coincides with the direction of gravity. Take element E_1 shown in Fig. 2b as an example, the pore pressure is assumed to obey a linear distribution, and fluid flow occurs when the head of the master Node m_1 differs from its neighboring master nodes. Then, the head gradient of master Node m_1 can be kept as a constant (Itasca, 2005; Yan et al., 2018)

$$\frac{\partial h}{\partial x_i} = \frac{1}{A} \sum_{n=1}^{3} \overline{h}^n \in_{ij} l_j^n \tag{7}$$

where A is the area of the triangle element, $\overline{h}^n$ is the average total water head on edge n, l_j^n is the coordinate difference between the two nodes of edge n, and $\in_{ij}$ is the two-dimensional matrix, i.e.,

$$\in_{ij} = \begin{bmatrix} 0 & 1 \\ -1 & 0 \end{bmatrix} \tag{8}$$

Equation (6) shows that even when the pore pressure of master Node m_1 is zero, the total head will still change due to gravity, which no doubt yields an unreasonable result. To circumvent this, we adopt a function f_s to modify Eq. (5), i.e.,

$$q_i = -\rho_f g \frac{k_{ij}}{\mu_f} \frac{\partial h}{\partial x_j} f_s \tag{9}$$

where

$$f_s = s^2(3 - 2s) \tag{10}$$

s is the saturation of the master node. Then, the fluid flow into master Node m_1 induced by slave Node 0 can be obtained by

$$Q_{m_1 \leftarrow 0} = -\frac{q_i n_i^{(0)} L^{(0)}}{2} \tag{11}$$

where $n_i^{(0)}$ is the outer normal unit vector of the edge opposite to slave Node 0, and $L^{(0)}$ denotes the length of the edge. Similarly, the total fluid flux of master Node m_1 contributed by its corresponding slave nodes is given by

$$Q_{m_1} = \sum_{k=0}^{5} Q_{m_1 \leftarrow k} \tag{12}$$

Within the updated fluid flow, the change of pore pressure at master Node m_1 is obtained by

$$\Delta P^t = \frac{M_b (Q_{m_1} \Delta t_{fp} - \Delta V)}{V^t} \tag{13}$$

where Δt_{fp} is the pore seepage timestep, V^t is the total volume by summating the 1/3 triangle element associated with the slave nodes, and ΔV is the volume change of the pore matrix through mechanical calculation (i.e., the difference between the current and the previous total volume). At the end of each iteration, the pore pressure of all slave nodes in the

same group needs to be synchronized like their master node. To ensure the stability of the numerical model, the timestep of pore seepage should be smaller than the critical value specified by

$$\Delta t_{\mathrm{fp}} \leqslant \frac{V}{M_{\mathrm{b}} \sum_i \frac{k_i}{\mu_{\mathrm{f}}}} \tag{14}$$

where V is the minimum volume of the pore node, and k_i is the isotropic intrinsic permeability.

Upon the breakage of a cohesive element, i.e., the generation of a new fracture, the master–slave node mapping list related to pore seepage needs to be updated. This update aims to ensure independent computation of pore seepage of the two finite elements located along the two sides of the new fracture, i.e., the fluid flux and pressure across the fracture are dependent without sharing common physical information (e.g., fluid pressure). Continuing with the example shown in Fig. 2 and focusing on the master Nodes m_1 and m_2, once the breakage of cohesive elements between Elements E_4 and E_5, E_2 and E_3, E_7 and E_8 occurs (see Fig. 3a), the connection between the slave nodes (e.g., Nodes 3 and 4, Nodes 1 and 2, Nodes 10 and 11, and Nodes 6 and 7) will be cut out. Then, each of the previous circle linked lists corresponding to master Nodes m_1 and m_2 becomes two open linked lists (i.e., the circle linked list on the left becomes $4 \rightarrow 5 \rightarrow 0 \rightarrow 1$ and $2 \rightarrow 3$; the circle linked list on the right becomes $7 \rightarrow 8 \rightarrow 9 \rightarrow 10$ and $11 \rightarrow 6$; see Fig. 3b). Each of the newly generated linked lists will be mapped to the new master nodes (e.g., m_3 and m_4 in Fig. 3b). Based on the updated master–slave list, the fluid flux and nodal masses of slave nodes in each group are all accumulated to their master node. Through the above procedure, we can guarantee the smooth transition of pore seepage from continuous to discontinuous using the node binding scheme when fracturing occurs. Note that the overall master–slave list only needs to be established before the onset of simulation, and it will be updated when cohesive element breakage occurs.

3.3. Fracture seepage model

We continue using the model in Fig. 3a to illustrate the implementation process of the fracture seepage model. As shown in Fig. 4a, three cohesive elements (C_1, C_2 and C_3, shaded in light blue) are broken when the cohesive tractions drop to the breakage point shown in Fig. 1, and fracture seepage is performed in those broken cohesive elements. Note that the broken cohesive elements represent the generation of fractures in FDEM, and we view each broken cohesive element as a fluid channel connected by two fluid cavities at its two ends. Each cavity represents a fluid reservoir and stores uniform fluid pressure. (e.g., cavity Nodes n_1 and n_2 in Fig. 4a). The fracture seepage model obeys the cubic law, and fluid will flow into the neighboring cavities through the fluid channel due to pressure difference. For the broken cohesive element C_2, we can obtain the total pressure difference between cavity Nodes n_1 and n_2, i.e.,

$$\Delta P = P_2 - P_1 + \rho_{\mathrm{f}} g (y_2 - y_1) \tag{15}$$

where P_1 and P_2 are the fluid pressures inside cavity Nodes n_1 and n_2, respectively, y_1 and y_2 are the elevations of cavity Nodes n_1 and n_2, respectively, g is the gravitational acceleration (in $-y$ direction), and ρ_{f} is the fluid density. Similar to the pore seepage, we also adopt the coefficient f_s, a function of the degree of saturation s, to modify the flow rate. Based on the cubic law, the fluid flow rate from cavity Nodes n_1 to Node n_2 is obtained by (Lisjak et al., 2017)

$$\begin{cases} q = -f_s \dfrac{(a_1 a_2)^2 \Delta P}{6\mu_{\mathrm{f}}(a_1 + a_2) L} \\ f_s = s^2(3 - 2s) \end{cases} \tag{16}$$

where a_1 and a_2 are the fracture apertures at the two endpoints of the fluid channel, L is the length of the fluid channel, μ_{f} is the fluid viscosity, s denotes the saturation of the cavity node, and the coefficient f_s is a function of the degree of saturation. Here

$$\begin{cases} a_1 = a_0 + o_1 \\ a_2 = a_0 + o_2 \end{cases} \tag{17}$$

where a_0 is the initial aperture value assigned to the flow channel that determines the initial permeability ($a_0/12$) of fracture seepage (He et al., 2022; Yang et al., 2022), o_1 and o_2 are the normal opening displacement of the two endpoints of a broken cohesive element (C_2). Additionally, the fracture aperture is assumed to have lower and upper bounds (a_{r} and a_{t}), where the lower bound is selected to avoid zero-division error in the computation. Since the fluid flow velocity is proportional to the square of the fracture aperture, the fluid flow along the fracture fails to ensure a laminar state when the fracture aperture is significantly large, which violates the basic assumption of cubic law. To address this issue, we borrow strategies from previous literature (Cai et al., 2022; Duan et al., 2021; Yan et al., 2023; Yan and Zheng, 2016), and set the upper bound of fracture aperture to avoid fast fluid flow. The fluid pressure of the cavity node can be obtained by

$$P^t = \begin{cases} P^{t-1} + K_{\mathrm{w}} \dfrac{Q \Delta t_{\mathrm{ff}}}{V^t} - K_{\mathrm{w}} \dfrac{2(V^t - V^{t-1})}{V^t + V^{t-1}} & s = 1 \\ 0 & 0 \leqslant s < 1 \end{cases} \tag{18}$$

Here,

$$Q = \sum_{i=0}^{i=k} q_i \tag{19}$$

where P^t and P^{t-1} are the current and previous fluid pressure at the cavity node, respectively, K_{w} denotes the bulk modulus of fluid, Q is the total flow at the cavity node, V^t and V^{t-1} are the current and previous volumes of the cavity node, respectively, and Δt_{ff} is fracture seepage timestep, k denotes the number of fluid channels that connect the fluid cavity, q_i is the fluid flow rate between adjacent fluid cavity nodes calculated by Eq. (16). Note that if $P^t < 0$, we will set $P^t = 0$ and update

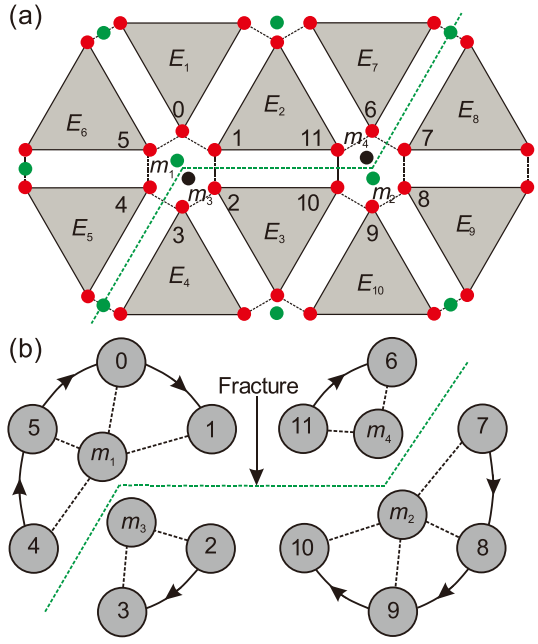

Fig. 3. Schematics for updating the master–slave node mapping list and the slave node group linked lists when breakage of pre-inserted cohesive elements occurs. Nodes m_3 and m_4 are new master nodes induced by broken cohesive elements.

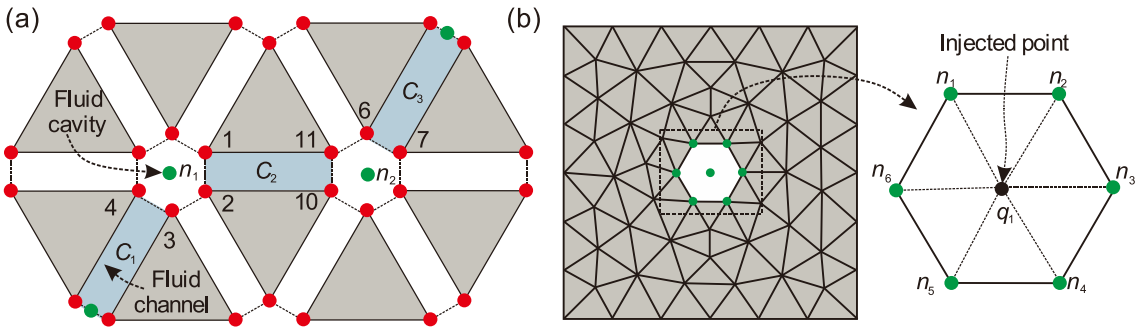

Fig. 4. (a) Discretization of fracture seepage model. Three broken cohesive elements are denoted as C_1, C_2 and C_3, respectively, which can also be regarded as fluid channels. The number of fluid cavities is represented by the cavity Nodes n_1 and n_2. (b) Boundary condition for constant injected rate in terms of hydraulic fracturing.

the saturation of the cavity node by

$$s = s_0 + \frac{Q\Delta t_{\mathrm{ff}}}{V^t} - \frac{2\left(V^t - V^{t-1}\right)}{V^t + V^{t-1}} \tag{20}$$

where s_0 is the initial saturation. A similar process is repeated for the broken cohesive elements C_1 and C_3. Then, the fracture fluid pressure of the computational domain will be updated in each timestep. To ensure the numerical stability of fracture seepage calculation, the timestep of the fracture seepage model, Δt_{ff}, must not exceed the threshold

$$\Delta t_{\mathrm{ff}} \leqslant \frac{V}{K_{\mathrm{w}} \sum_i \frac{a_i^3}{12\mu_{\mathrm{f}}}} \tag{21}$$

According to Eq. (21), we can obtain that the timestep of the fracture seepage model is inversely proportional to the cubic power of fracture aperture. Consequently, we can dynamically adjust the timestep based on the variance of fracture aperture. For example, when the fracture aperture is small or the number of fractures is limited, the fracture seepage timestep Δt_{ff} should be appropriately increased to minimize the computational cost. However, the timestep of the fracture seepage model is far smaller than that of pore seepage due to its high dependence on fracture aperture. Therefore, it is challenging to overcome this dependence and increase computational efficiency in practical rock engineering problems in the near future. It is worth noting that we need to re-number the partial cavity nodes associated with fluid injection boundaries when a constant injection rate of fluid is used for hydraulic fracturing. For the example shown in Fig. 4b, the fracture pressure and flux of cavity Nodes n_1 to n_6 are identical during the hydraulic fracturing, and thus these cavity nodes need to be re-numbered as the same cavity node q_1.

3.4. Fluid exchange between fracture and solid rock matrix

We take the model shown in Fig. 5 as an example to elucidate the process of fluid exchange between fracture and solid rock matrix, where the rock matrix is cut into two equal parts by fracture. As illustrated in Fig. 5, the fluid pressure stored in the fracture is denoted as P_{f}; the pore pressure of the rock matrix at both sides of the fracture is represented by P_{p}^{+} and P_{p}^{-} respectively; L is the fracture length. Then, the fluid flow exchange per unit time between the fracture and rock matrix on the left (Q_{ex}^{+}) and the right (Q_{ex}^{-}) side of the interface is given by:

$$Q_{\mathrm{ex}}^{+} = h_{\mathrm{c}}\left(P_{\mathrm{p}}^{+} - P_{\mathrm{f}}\right)L \tag{22}$$

and

$$Q_{\mathrm{ex}}^{-} = h_{\mathrm{c}}\left(P_{\mathrm{p}}^{-} - P_{\mathrm{f}}\right)L \tag{23}$$

where h_{c} is the fluid exchange coefficient between the fracture and rock matrix. Then, the exchanged fluid flow will be incorporated into Eqs. (13) & (18) respectively, thereby updating the fluid pressure of rock matrix and fracture. Additionally, we assume that the pressure variance induced by fluid flux exchange should not exceed the pressure difference between fracture and pore seepage nodes, i.e.,

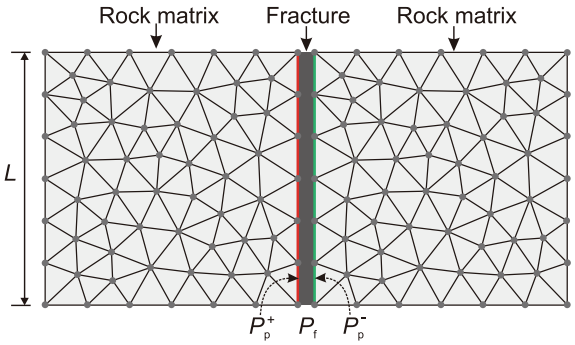

Fig. 5. Fluid exchange between fracture and rock matrix. P_{f} is the fluid pressure of fracture; P_{p}^{+} and P_{p}^{-} are the pore pressure of the rock matrix at two sides of a fracture, which are marked in red and blue lines, respectively. (For interpretation of the references to colour in this figure legend, the reader is referred to the web version of this article.)

$$M_{\mathrm{b}}\frac{\left|Q_{\mathrm{ex}}^{+}\right|\Delta t_{\mathrm{fp}}}{V^{\mathrm{p}}} \leqslant \left|P_{\mathrm{p}}^{+} - P_{\mathrm{f}}\right| \tag{24}$$

and

$$K_{\mathrm{w}}\frac{\left|Q_{\mathrm{ex}}^{+}\right|\Delta t_{\mathrm{ff}}}{V^{\mathrm{f}}} \leqslant \left|P_{\mathrm{p}}^{+} - P_{\mathrm{f}}\right| \tag{25}$$

where V^{p} and V^{f} are the volume of pore and fracture fluid nodes, respectively. Then, we can further obtain the upper limit of h_{c} according to Eqs. (24) & (25)

$$h_{\mathrm{c}} \leqslant \min\left(\frac{V^{\mathrm{p}}}{M_{\mathrm{b}}\Delta t_{\mathrm{fp}}L}, \frac{V^{\mathrm{f}}}{K_{\mathrm{w}}\Delta t_{\mathrm{ff}}L}\right) \tag{26}$$

3.5. Hydro-mechanical coupling

3.5.1. Pore pressure

Based on Biot's theory (see Fig. 6a), the updated pore pressure can produce the variation of stress field ($\Delta\sigma_{ij}$) within triangle elements (Yan et al., 2018), i.e.,

$$\Delta\sigma_{ij} = -\alpha P_{\mathrm{ave}}\delta_{ij} \tag{27}$$

where P_{ave} is the pore pressure of a triangle element that can be obtained by averaging the three nodal pore pressures, and δ_{ij} is the Kronecker delta. The sign convention of tension as positive is used here. Then, the stress increment can be further applied to the nodes of the triangle

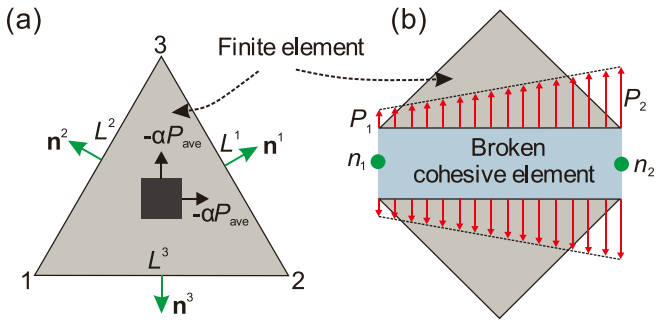

Fig. 6. (a) Pore and (b) fracture pressure are applied on two triangle elements. $\mathbf{n}^1$, $\mathbf{n}^2$ and $\mathbf{n}^3$ are the unit outward normal vectors of the three edges of a triangle element, L^1, L^2 and L^3 are the lengths of the three edges of the triangle element, P_1 and P_2 are the fracture fluid pressure at the cavity Nodes n_1 and n_2, respectively.

elements (Yan et al., 2018), i.e.,

$$\left(f_{\mathrm{p}}\right)_i^k = -\frac{\alpha P_{\mathrm{ave}} L^k}{2} n_i^k \quad (i = 1,2 \quad k = 1,2,3) \tag{28}$$

where n_i^k and L^k are the outward unit normal vector and length of the edge facing node k (see Fig. 6a). Note that Eq. (28) only considers the infinitesimal strain theory where the displacements and rotation of the solid body are assumed to be much smaller than any relevant dimension of the body. Previous work has successfully incorporated the finite-strain theory into the thermo-mechanical (TM) coupling approach (Joulin et al., 2020; Wang et al., 2021). Therefore, to deal with large displacements and rotations induced by pore pressure, it is necessary to adopt the finite-strain theory that is consistent with the FDEM framework to consider the mechanical response from pore seepage in future work.

3.5.2. Fracture pressure

As shown in Fig. 6b, the fracture pressures of cavity Nodes n_1 and n_2 are denoted as P_1 and P_2, respectively. Then, the total normal fluid pressure acting on the two sides of the finite elements connected by the broken cohesive element can be given by

$$\begin{cases} f_1 = \dfrac{L}{6}(2P_1 + P_2) \\ f_2 = \dfrac{L}{6}(2P_2 + P_1) \end{cases} \tag{29}$$

where f_1 and f_2 are the equivalent nodal force at the two endpoints of the fluid channel, respectively; L is the length of fluid channel. According to the previous work (Yan and Zheng, 2016), the total tangential fracture pressure acting on the two sides of the finite elements is given by

$$f_{\mathrm{c}} = \frac{a_1 + a_2}{4}(P_1 - P_2) \tag{30}$$

Since the fracture aperture ($\sim 10^{-3}$ m to 10^{-5} m) is relatively small compared to the size of finite element, the tangential viscous force is not considered in the subsequent related works (Lisjak et al., 2017; Wu et al., 2022; Yan et al., 2018), nor in the current paper.

3.5.3. Coupling scheme

The simulation workflow of hydro-mechanical coupling is illustrated in Fig. 7. The mechanical solver starts first, followed by the solvers for pore and fracture seepage, respectively. At the end of each iteration, the total nodal force obtained by accumulating the Cauchy stress, cohesive tractions, pore and fracture pressure (Eqs. (28) & (29)) will be employed to explicitly update the nodal displacements and velocities based on Newton's second law. Each physical solver has a corresponding critical timestep, which must guarantee the stability of numerical models. Generally, the minimum of the above three critical timesteps is used, which no doubt yields a significant computational cost. Therefore, we use different timesteps for the mechanical solver, pore seepage model and fracture seepage model in our proposed coupling model according to Eqs.(14) & (21). The pore-fracture seepage model mainly consists of frequent updating of the fluid flow and pressure at each node. The updated fluid pressure is resolved to the nodes of finite elements, thereby producing the mechanical response of the solid domain. When the breakage of a cohesive element occurs, we need to update the fracture aperture and establish fluid channels and cavities for the fracture seepage model. For the pore seepage model, the broken cohesive element will invoke the update of the master–slave list. In addition, the deformation of triangle elements can also affect the volume of the pore seepage node. Upon this process, we can achieve the hydro-mechanical coupling model in FDEM, which provides an effective way to simulate the process of fluid-driven fracturing.

It is worth noting that the damage process of cohesive elements may affect the fluid flow. However, previous works in the FDEM community mainly activate the flow channel of fracture seepage model when the "cohesive elements" are completely broken (Lisjak et al., 2017; Wu et al., 2022; Yan et al., 2018; Yan and Zheng, 2016). Here, two aspects may support our consideration, i.e., (i) the process of cohesive tractions from peak strength to breakage point is relatively small compared to the simulated time, thus the effect of cohesive element damage on fluid flow is not considered; (ii) near the fracture tips, although no broken cohesive elements serve as fluid channels, fluid flow still occurs through pore

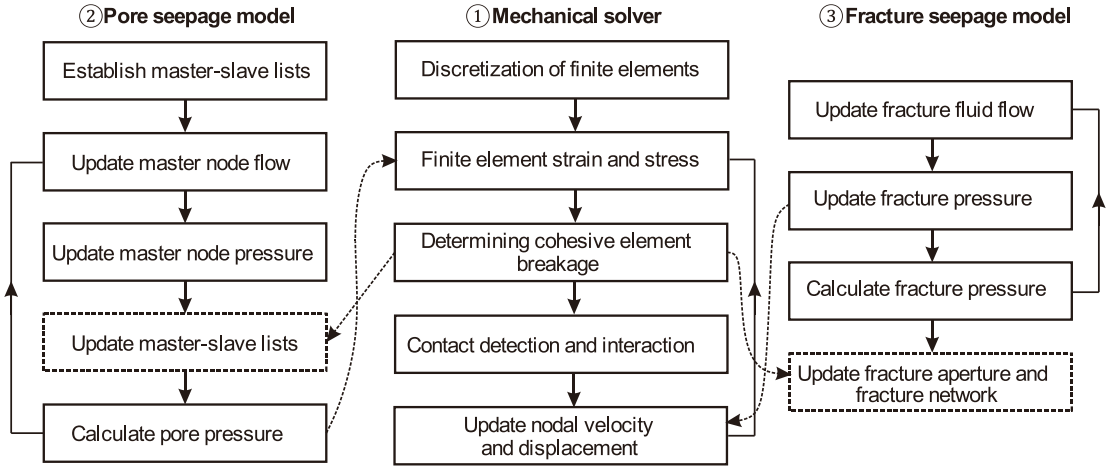

Fig. 7. Simulation workflow of hydro-mechanical coupling.

seepage. Additionally, the discontinuity of fluid pressure for the regions where the governing equation changes from Darcy's flow to channel flow can be effectively eliminated through the fluid flow exchange between fluid and solid. More benchmark examples are performed in the next section to verify the accuracy and robustness of the hydro-mechanical model.

4. Verification and comparison

This section presents eight numerical examples to verify the accuracy of the unified pore-fracture seepage model in the current FDEM, and to demonstrate its capability of simulating fluid-driven fractures and advantage in computational efficiency. Note that the initial node saturation is set to unity in all numerical cases.

4.1. Pore seepage

4.1.1. Steady-state pore seepage in hollow cylinder

A thick-wall cylinder with inner radius $r_i = 0.05$ m and outer radius $r_o = 0.5$ m (see Fig. 8a) is employed to verify the accuracy of pore seepage under steady state. The cylinder is assumed to be homogeneous and isotropic. P_i (2 MPa) and P_o (1 MPa) represent the fixed pressure at the inner and outer boundary of the cylinder, respectively. Note that the deformation and fracturing of the cylinder are not considered in this case. The analytical solution for the pore pressure distribution in the thick-wall cylinder is given by (Fjær et al., 2008)

$$P = P_i + \frac{P_o - P_i}{\ln(r_o/r_i)} \ln\left(\frac{r}{r_i}\right) \tag{31}$$

where r is the distance from the monitoring point to the cylinder center. The model input parameters are tabulated in Table 1. The model consists of 14,062 triangle elements with an average element size of 0.012 m, and the total simulation time is 0.24 s. Note that the viscous damping coefficient of finite elements is calculated by the equation $\eta = 2h\sqrt{E\rho}$ (E is Young's modulus and ρ is bulk density) for all numerical cases (Tatone and Grasselli, 2015), which aims to circumvent the high-frequency wave effect (with high oscillation). It is worth noting that the local damping with a mass scaling technique implemented by Fukuda et al., (2019a) can be employed to overcome the low-frequency wave effect. The final pore pressure distribution in the thick-wall cylinder is shown in Fig. 8b, manifesting a gradual decrease from inside to outside. The maximum error between the FDEM (without DEM) simulated result and the analytical solution with respect to the pore pressures at locations with equal radial distance from the model center is $\sim 4.6 \times 10^{-4}$ MPa (see Fig. 8c), thus verifying the accuracy of the proposed approach for pore seepage simulation in elastic media.

Table 1
Input parameters in FDEM (without DEM) for steady-state pore seepage simulations.

Input parameters	Values
Young's modulus, E (GPa)	30
Bulk density, ρ (kg/m^3)	2550
Poisson's ratio, ν	0.2
Viscous damping coefficient, η (kg/m·s)	8900
Normal contact penalty, P_n (GPa)	300
Tangential contact penalty, P_s (GPa)	300
Fluid viscosity, μ_f (Pa·s)	1.0×10^{-3}
Fluid density, ρ_f (kg/m^3)	1000
Intrinsic permeability, k (m^2)	1.0×10^{-12}
Biot's modulus, M_b (GPa)	22
Porosity, ψ (−)	0.1
Solid timestep, Δt_s (s)	2.9×10^{-7}
Pore seepage timestep, Δt_{fp} (s)	6.0×10^{-6}

4.1.2. Fluid pressure distribution in transient states

To verify the accuracy of pore seepage in a transient state, we construct a rectangular plate model with dimensions of 1 m × 0.25 m (length × width). The left and right boundaries of the model are exposed to two constant pore pressures of P_L (0 MPa) and P_R (1 MPa), respectively, whereas its bottom and top boundaries are impermeable. The model consists of 4556 triangle elements with an average element size of 30 mm (see Fig. 9a), and the input parameters are tabulated in Table 2. A horizontal monitoring line marked in blue with $y = 0$ is set in the model's center to track the pore pressure evolution via time, and the deformation and fracturing of the model are not considered here. The analytical solution for pore pressure is a function of x (distance from the left boundary) and t (time) as (Crank, 1975)

$$P(x,t) = P_L + (P_R - P_L)\frac{x}{l} + \frac{2}{\pi}\sum_{n=1}^{\infty}\frac{P_R\cos n\pi - P_L}{n}\sin\frac{n\pi x}{l}\exp\left(-\kappa n^2\pi^2 t/l^2\right) + \frac{4P'}{\pi}\sum_{m=0}^{\infty}\frac{1}{2m+1}\sin\frac{(2m+1)\pi x}{l}\exp\left(-\kappa(2m+1)^2\pi^2 t/l^2\right) \tag{32}$$

where P' is the initial pore pressure of all elements and is set to zero, and l is the length of the model; κ is the pore pressure diffusivity and given by

$$\kappa = k/\left(\mu_f\right)M_b \tag{33}$$

where k is the intrinsic permeability, μ_f is the fluid viscosity, and M_b is the Biot modulus.

The pore pressure distributions at different timestamps (0.1 ms, 0.5 ms and 2 ms) in Fig. 9b show that the pore pressure gradually increases from the left to the right side of the plate. The maximum error between

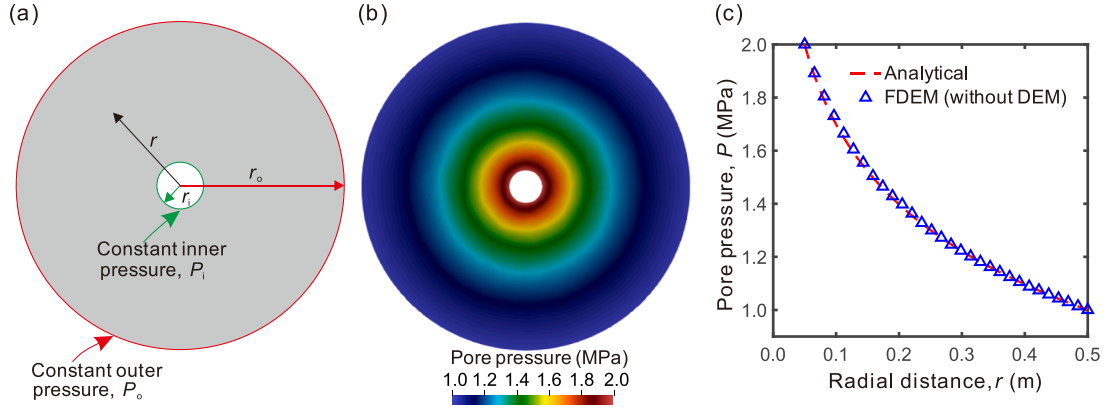

Fig. 8. Steady-state radial pore pressure in a hollow cylinder. (a) Geometry and boundary conditions of the model. (b) Pore pressure distribution in the cylinder. (c) Comparison between analytical and FDEM (without DEM)-simulated radial pore pressure distribution.

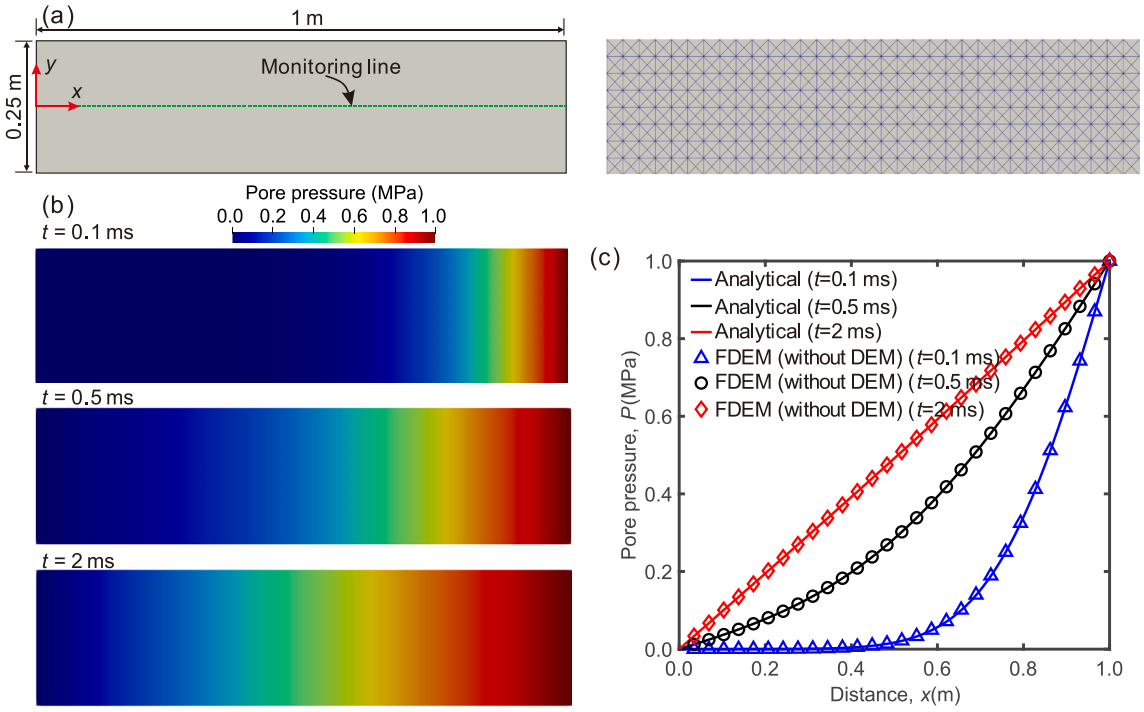

Fig. 9. (a) Model geometry and mesh (The blue dotted line is the monitoring line). (b) Pore pressure distribution at various timestamps: 0.1 ms, 0.5 ms and 2 ms. (c) Comparison between analytical and FDEM (without DEM) results in terms of pore pressure distribution along the monitoring line. (For interpretation of the references to colour in this figure legend, the reader is referred to the web version of this article.)

Table 2
Input parameters in FDEM (without DEM) simulations for transient pore seepage.

Input parameters	Values
Young's modulus, E (GPa)	30
Bulk density, ρ (kg/m^3)	2700
Poisson's ratio, ν	0.27
Viscous damping coefficient, η (kg/m·s)	2.7×10^5
Normal contact penalty, P_n (GPa)	300
Tangential contact penalty, P_s (GPa)	300
Fluid viscosity, μ_f (Pa·s)	1.0×10^{-3}
Fluid density, ρ_f (kg/m^3)	1000
Intrinsic permeability, k (m^2)	1.0×10^{-11}
Biot modulus, M_b (GPa)	22
Porosity, ψ (−)	0.1
Solid timestep, Δt_s (s)	9.0×10^{-7}
Pore seepage timestep, Δt_{fp} (s)	1.0×10^{-7}

the FDEM (without DEM) simulated result and the analytical solution with respect to pore pressure distribution along the monitoring line is ~ 3.9×10^{-8} MPa (see Fig. 9c), which demonstrates the correctness of the proposed approach for seepage flow simulation under a transient state.

4.2. Fracture seepage

4.2.1. Flow along a pre-existing fracture

To verify the accuracy of fracture seepage, we establish a rectangular plate with a constant and uniform aperture (see Fig. 10a), and its dimensions are 1 m × 0.20 m (length × width). A constant pressure P_0 (5 MPa) is applied to the left boundary of the plate, whereas the right boundary is impermeable. The model is assumed to be an impermeable rock in the continuous domain and consists of 2000 triangle elements with an average element size of 20 mm (see Fig. 10b). The analytical solution for fracture fluid pressure at a specific point is given by (Carslaw and Jaeger, 1959)

$$P = P_0\left\{1+\frac{4}{\pi}\sum_{n=0}^{\infty}\left[e^{\frac{-(2n+1)^2T\pi^2}{4}}\cos\left(\frac{(2n+1)\pi\xi}{2}\right)\left(\frac{(-1)^{n+1}}{2n+1}\right)\right]\right\} \tag{34}$$

Here,

$$\begin{cases} T = \dfrac{K_w a_0^2 t}{12\mu_f L^2} \\ \xi = (L-x)/L \end{cases} \tag{35}$$

where K_w is the bulk modulus of the fluid, μ_f denotes the fluid viscosity, a_0 is the initial fracture aperture, L is the fracture length, t is the time of fracture seepage, and x is the distance from a point to the left boundary of the plate. The input parameters are tabulated in Table 3, and the deformation and fracturing of the plate are not considered by fixing the nodal displacements and velocities to zero. To compare the fluid pressure distribution along the fracture between the FDEM (without DEM) simulated and the analytical results, we select five equally spaced monitoring points (i.e., points A, B, C, D and E in Fig. 10a) to obtain the fluid pressure evolution with time (t). The fluid pressure distribution at 40 ms is shown in Fig. 10c, demonstrating a gradually decreased fluid pressure along the fracture from the left to the right boundary of the plate. As illustrated in Fig. 10d, the maximum error between the FDEM (without DEM) simulated result and the analytical solution with respect to the temporal variation of the simulated fluid pressure at the five monitoring points is ~ 4.5×10^{-6} MPa, verifying the correctness of the proposed approach for fracture seepage simulation.

4.2.2. Fluid-pressurized discontinuity in rock mass with pre-existing fracture

A homogeneous and isotropic rock model with dimensions of 100 m × 100 m (width × height) is established to verify the accuracy of coupled response between fluid and solid (Fig. 11a). The rock contains a 20 m long pre-existing fracture in the middle with zero initial aperture.

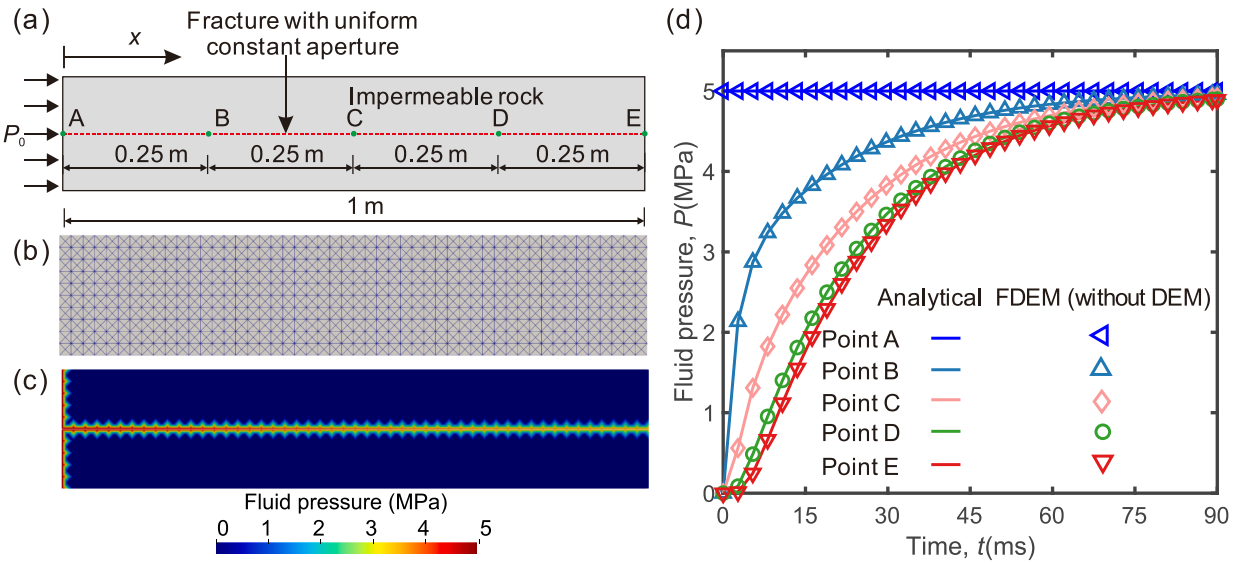

Fig. 10. (a) Model geometry and boundary conditions (The monitoring points are marked by green dots, i.e., Points A, B, C, D and E). (b) Mesh. (c) Fluid pressure distribution at 40 ms. (d) Comparison between analytical and FDEM (without DEM) simulated fluid pressure evolution at the five monitoring points along the fracture. (For interpretation of the references to colour in this figure legend, the reader is referred to the web version of this article.)

Table 3
Input parameters in FDEM (without DEM) simulations for fracture seepage.

Input parameters	Values
Young's modulus, E (GPa)	30
Bulk density, ρ (kg/m^3)	2550
Poisson's ratio, ν	0.2
Viscous damping coefficient, η (kg/m·s)	1.7×10^5
Normal contact penalty, P_n (GPa)	300
Tangential contact penalty, P_s (GPa)	300
Fluid viscosity, μ_f (Pa·s)	1.0×10^{-3}
Bulk modulus of the fluid, K_w (GPa)	2.2
Fluid density, ρ_f (kg/m^3)	1000
Initial aperture, a_0 (m)	1.0×10^{-5}
Minimum aperture, a_r (m)	1.0×10^{-5}
Maximum aperture, a_t (m)	1.0×10^{-5}
Fracture seepage timestep, Δt_{ff} (s)	1.2×10^{-7}

The internal fluid pressure applied on the fracture surfaces is increased gradually from 0 to a prescribed value $P = 20$ MPa over a time span of 1×10^{-3} s. For simplicity, rock specimens are assumed to be elastic and impermeable and do not allow damage or fracturing, i.e., we only consider their elastic deformation. The model consists of 30,006 triangle elements with an average element size of 0.15 m, and the timestep of the rock domain is 7.2×10^{-6} s. The mesh around the pre-existing fracture is refined (average element size of 0.06 m), and the unstructured Delaunay triangulation mesh scheme is employed (see Fig. 11b). The following key rock parameters are used in the model: Young's modulus $E = 40$ GPa, bulk density $\rho = 2700$ kg/m^3, Poisson's ratio $\nu = 0.22$, and viscous damping coefficient of finite element $\eta = 2.9 \times 10^6$ kg/m·s.

The analytical solution for the aperture along the fracture under plane stress conditions can be found in Lisjak et al. (2017), i.e.,

$$\delta(x) = \frac{4P(1-\nu^2)}{E}\left(L^2 - x^2\right) \tag{36}$$

where $L = 10$ m is the half-length of the pre-existing fracture, and x represents the horizontal distance from the fracture center. The center of the specimen coincides with the origin of the x-y coordinate system (see the green dot in Fig. 11a). Upon the model reaching equilibrium, the apertures along the fracture are extracted to compare the numerical and analytical results. As shown in Fig. 11c, the maximum error between the FDEM (without DEM) simulated result and the analytical solution with respect to fracture aperture is ~ 0.08 mm, demonstrating the correctness of the proposed approach for hydro-mechanical coupling simulation.

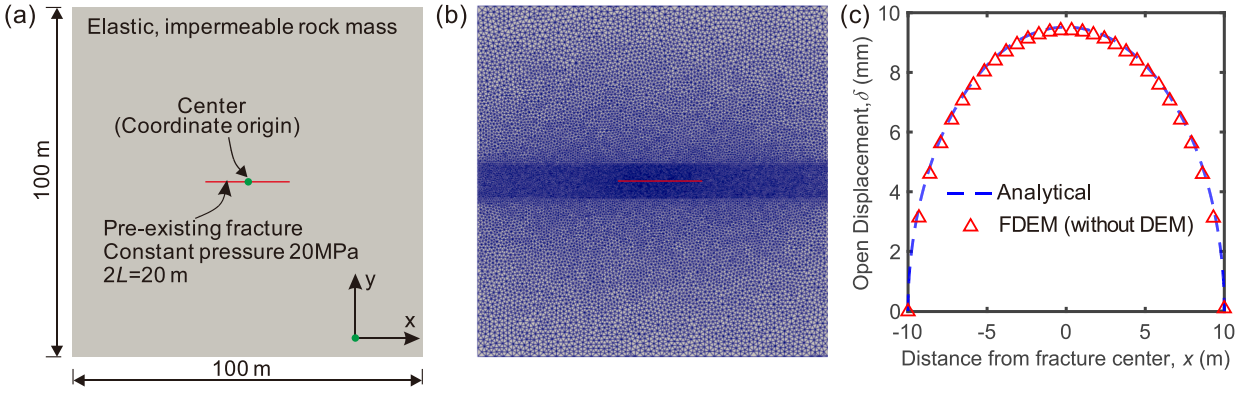

Fig. 11. (a) Model geometry and boundary conditions (The coordinate origin is marked by a green dot). (b) Mesh. (c) Comparison between analytical and FDEM (without DEM) simulated fracture aperture along the pre-existing fracture. (For interpretation of the references to colour in this figure legend, the reader is referred to the web version of this article.)

4.3. Pore-fracture seepage

To verify the robustness of the proposed unified pore-fracture seepage model, we establish a rectangle plate containing one inclined-through fracture with a slope of 0.3:1 to simulate the fluid seepage in the fractured porous rock mass. The plate has dimensions of 1 m × 0.5 m (width × height) (see Fig. 12a). Constant fluid pressures $P_L = 9.5$ MPa and $P_R = 4.5$ MPa are applied on the left and right boundaries of the plate, respectively, and the initial pore pressure in the porous rock matrix is set as 0 MPa. The model consists of 9410 triangle elements with an average element size of 5.1 mm, and the unstructured Delaunay triangulation mesh scheme is employed (see Fig. 12a). Note that the deformation and fracturing of the plate are not considered. The key input parameters of the problem are tabulated in Table 4. Fig. 12 displays the fluid pressure distributions at different timestamps. This figure shows that the fluid pressure diffuses to the middle of the plate along the fracture and the rock matrix, and the seepage speed of fracture fluid is greater than that in the rock matrix. Besides, when the fracture fluid flow reaches a steady state, the fluid pressure begins to spread to the upper and lower sides of the plate. The fluid pressure evolution is consistent with the previous simulation (Ma, 2022), thus verifying the accuracy of the proposed approach for simulating fluid seepage in fractured porous media.

Table 4
Input parameters in FDEM (without DEM) simulations for the proposed unified pore-fracture seepage model.

Input parameters	Values
Young's modulus, E (GPa)	30
Bulk density, ρ (kg/m^3)	2700
Poisson's ratio, ν	0.25
Viscous damping coefficient, η (kg/m·s)	9.2×10^4
Fluid viscosity, μ_f (Pa·s)	1.0×10^{-3}
Fluid density, ρ_f (kg/m^3)	1000
Intrinsic permeability, k (m^2)	1.0×10^{-13}
Biot modulus, M_b (GPa)	11
Porosity, ψ (−)	0.2
Bulk modulus of the fluid, K_w (GPa)	2.2
Initial aperture, a_0 (m)	4.0×10^{-5}
Minimum aperture, a_r (m)	1.0×10^{-5}
Maximum aperture, a_t (m)	3.0×10^{-3}
Fluid exchange coefficient, h_c (m/Pa·s)	2.3×10^{-7}
Solid timestep, Δt_s (s)	3.0×10^{-7}
Fracture seepage timestep, Δt_{ff} (s)	3.0×10^{-9}
Seepage seepage timestep, Δt_{fp} (s)	1.2×10^{-8}

4.4. Fluid-driven fracture

4.4.1. Single fluid-driven fracture

A square plate containing a single fracture is constructed to demonstrate the capability of the proposed approach in simulating the single fluid-driven fracture propagation. The side length of the plate is 70.7 mm, with a pre-existing fracture of length $L = 15$ mm located at the center (see Fig. 13a). Vertical displacements are constrained for the lower and upper edges, and horizontal displacements are blocked for the lateral edges. The fluid pressure at the plate boundaries is maintained at 0 MPa, and the fluid is injected in the pre-existing fracture at a constant flow rate $Q = 0.002$ m^2/s. The model consists of 26,492 triangle elements with an average element size of 0.284 mm, and the unstructured Delaunay triangulation mesh scheme is employed (Fig. 13b). The input parameters of the problem are summarized in Table 5. The fracture propagation and fluid pressure distribution at different timestamps are shown in Fig. 13d-f. It can be seen that the newly generated cracks propagate roughly along the plane of the pre-existing fracture and finally split the model into two halves, which is consistent with previous experimental observation (Liu et al., 2018) (see Fig. 13c).

4.4.2. Parallel fluid-driven fractures

A square plate model containing two parallel and zero-initial-thickness fractures with an initial length of $L = 3$ m is utilized to validate the multiple fluid-driven fracture propagation simulation. The side length of the plate is 10 m, and the distance between the two parallel fractures is $d = 3$ m (see Fig. 14a). Vertical displacements are constrained for the lower and upper edges, and horizontal displacements are blocked for the lateral edges. The fluid is injected into the two pre-existing fractures from the bottom at a constant flow rate $Q = 0.01$ m^2/s. The model consists of 19,929 triangle elements with an average element size of 0.042 m, and the unstructured Delaunay triangulation mesh scheme is employed in Fig. 14b. The input parameters of the model are tabulated in Table 6. The simulated fluid-driven fracture propagation is presented in Fig. 14c-e. We can see new cracks are initiated from the tips of the pre-existing fractures and propagate toward the left and right sides of the plate, respectively. As fractures continue to propagate, the fluid pressure increases at places between the two fractures and induces a disturbance in the stress field around the fracture tip areas. The two cracks propagate symmetrically, and the final pattern is similar to the previous observation (Paul et al., 2018).

4.4.3. Hydraulic fracturing with borehole injection

A rock specimen with a borehole at its center with a radius of (r_0) 0.1 m is constructed to simulate borehole fluid injection (see Fig. 15a). The width and height of the specimen are 2 m, and the constant borehole injection rate is $Q = 0.004$ m^2/s. The horizontal and vertical in situ stress are applied on the boundaries of the rock specimen and are increased gradually from 0 to 4 MPa and 2 MPa over a time span of 3×10^{-4} s, respectively. The model consists of 25,967 triangle elements with an average element size of 7.76 mm, and the unstructured Delaunay triangulation mesh scheme is employed (Fig. 15a). To investigate the

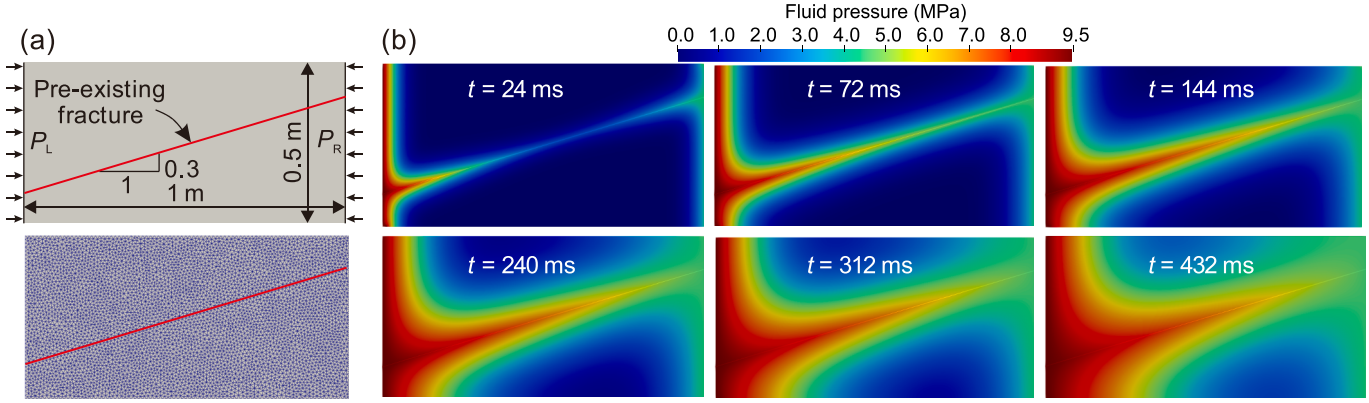

Fig. 12. (a) Model geometry and mesh. (b) Fluid pressure distribution in a porous media with an inclined fracture at different timestamps.

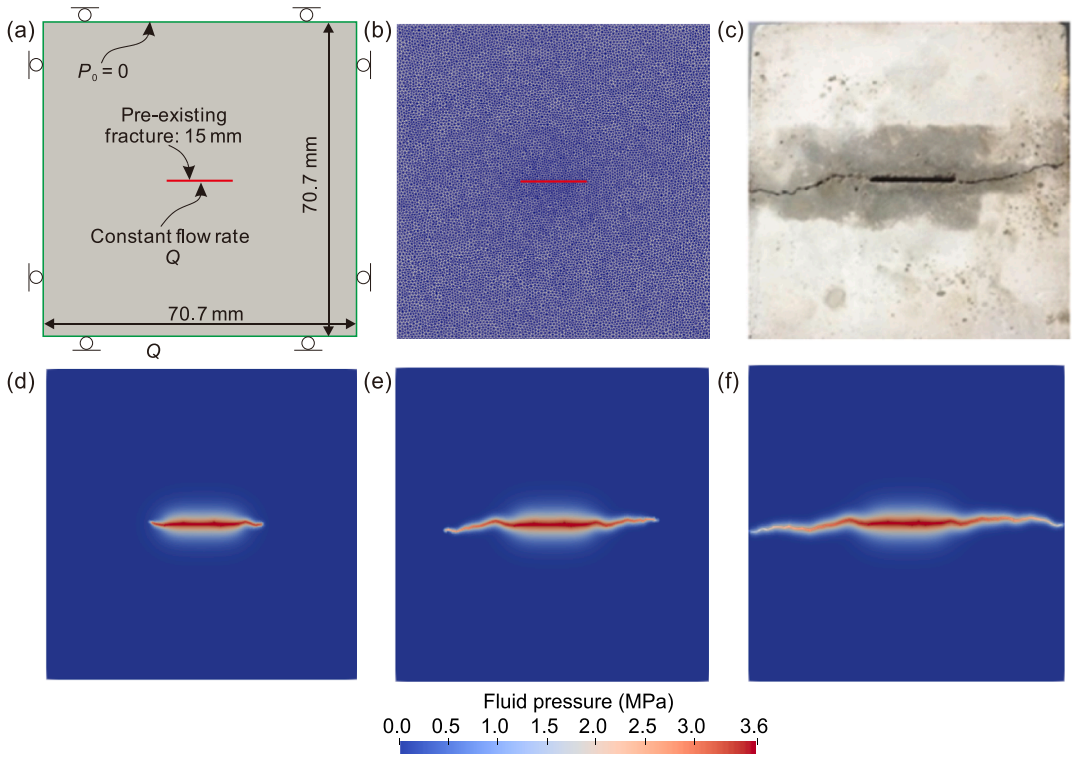

Fig. 13. (a) Model geometry and boundary conditions. (b) Mesh. (c) Experimental observation (Liu et al., 2018). Fluid pressure distribution at different timestamps: (d) $t = 4.75 \times 10^{-4}$ s, (e) $t = 5 \times 10^{-4}$ s and (f) $t = 5.25 \times 10^{-4}$ s.

Table 5
Input parameters in FDEM simulations for single fracture propagation.

Input parameters	Values
Young's modulus, E (GPa)	11.63
Bulk density, ρ (kg/m^3)	2380
Poisson's ratio, ν	0.20
Viscous damping coefficient, η (kg/m·s)	3000
Tensile strength, f_t (MPa)	3
Cohesion, c (MPa)	20
Internal friction angle, φ (°)	40
Mode I fracture energy, G_{f1} (J/m^2)	5
Mode II fracture energy, G_{f2} (J/m^2)	40
Normal contact penalty, P_n (GPa)	110
Tangential contact penalty, P_s (GPa)	110
Fluid viscosity, μ_f (Pa·s)	1.0×10^{-3}
Fluid density, ρ_f (kg/m^3)	1000
Intrinsic permeability, k (m^2)	1.0×10^{-13}
Biot modulus, M_b (GPa)	11
Porosity, ψ (−)	0.2
Initial aperture, a_0 (m)	5.0×10^{-5}
Minimum aperture, a_r (m)	1.0×10^{-5}
Maximum aperture, a_t (m)	3.0×10^{-4}
Fluid exchange coefficient, h_c (m/Pa·s)	1.1×10^{-6}
Solid timestep, Δt_s (s)	2.5×10^{-8}
Fracture seepage timestep, Δt_{ff} (s)	8.0×10^{-11}
Pore seepage timestep, Δt_{fp} (s)	5.0×10^{-10}

effect of fluid viscosity on hydraulic fracturing, we use a low viscosity fluid of $\mu_f = 0.1$ Pa•s and a high viscosity fluid of $\mu_f = 10$ Pa•s in this case. The key input parameters of the problem are tabulated in Table 7. The fluid pressure and fracture patterns using low and high viscosity fluid are respectively shown in Fig. 15b and Fig. 15c. It can be observed that the low viscosity fluid facilitates fluid diffusion into the rock matrix, and the fluid pressure in the newly generated fractures is obviously larger than that in the model using high viscosity fluid. Besides, the high fluid viscosity restricts fluid flow into hydraulic fractures, which leads to higher fluid pressure around the borehole vicinity. The low fluid viscosity is beneficial to hydraulic fracture propagation compared to high fluid viscosity, as reported in previous literature (Yan and Zheng, 2016).

4.5. Computational efficiency

As mentioned in Section 1, in previous FDEM-related works, a fluid exchange coefficient of cohesive elements has to be introduced to simulate pore seepage between adjacent finite element pairs (Yan and Jiao, 2018; Yan et al., 2022b). The numerical results obtained from such a pore seepage model can only approximate the analytical solution when an infinite fluid exchange coefficient is employed. However, a large fluid exchange coefficient can significantly reduce the computational efficiency of the pore seepage model. Additionally, an inappropriate fluid exchange coefficient specified may produce the instability of the seepage model. For convenience, this conventional pore seepage model using fluid exchange coefficient is named the "original approach" hereafter. To further compare the computational efficiency between the proposed and the original approaches, a rectangular plate with dimensions of 2 m × 0.3 m (length × width) is established to simulate the process of pore seepage under steady state (see Fig. 16a). Two constant pore pressure of P_L (0 MPa) and P_R (1.0 MPa) are applied to the left and right boundaries of the plate, respectively. The bottom and top boundaries of the plate are set to be impermeable. The key input parameters are tabulated in Table 8.

A variable r_{effi} is proposed to denote the ratio of the computing time needed between the original and the proposed approaches upon pore seepage reaching a steady state. The width of the plate and average element size are denoted as L and h, respectively, and increasing their ratio L/h represents an increase in the number of finite elements in the model. As shown in Fig. 16b, with the increase of L/h, the efficiency index r_{effi} increases drastically and reaches around 120 times for $L/h = 100$ (about 6000 triangle elements). Therefore, the proposed approach regarding pore seepage simulation in the intact/continuous deformation regime can effectively reduce computational costs compared to the

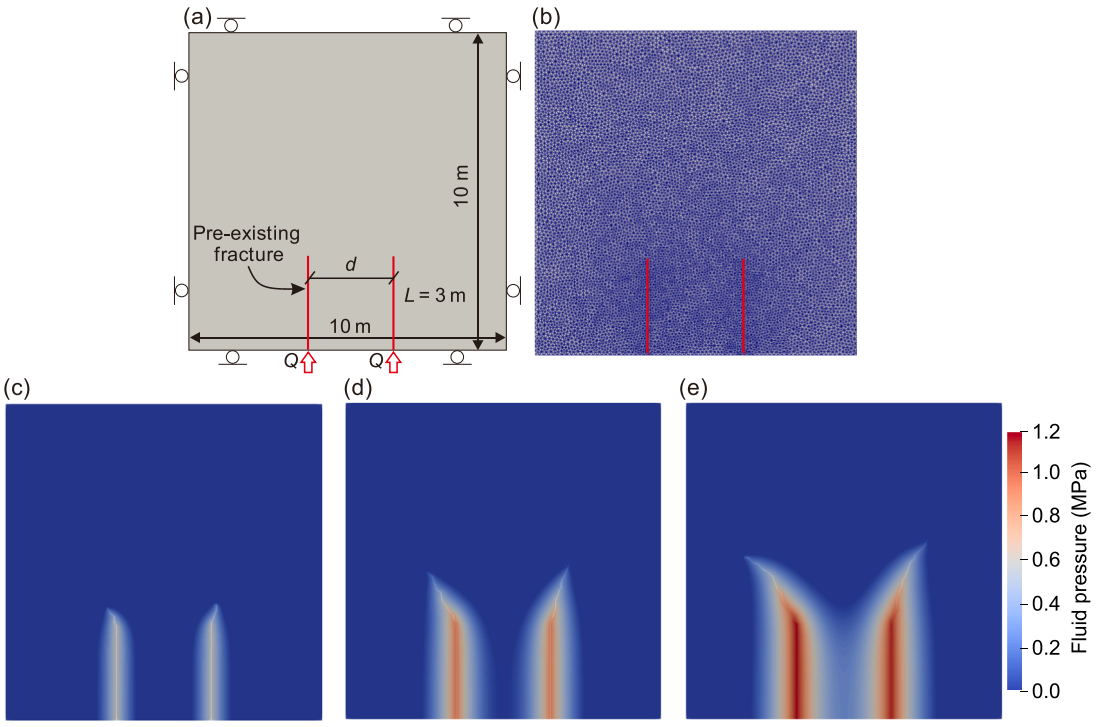

Fig. 14. (a) Model geometry and boundary conditions. (b) Mesh. Fluid pressure distribution under constant flow injection at the bottom of the two pre-existing fractures at different timestamps: (c) $t = 0.06$ s, (d) $t = 0.14$ s and (e) $t = 0.2$ s.

Table 6
Input parameters in FDEM simulations for two parallel fractures propagation.

Input parameters	Values
Young's modulus, E (GPa)	16
Bulk density, ρ (kg/m^3)	2000
Poisson's ratio, ν	0.20
Viscous damping coefficient, η (kg/m·s)	4.7×10^5
Tensile strength, f_t (MPa)	3
Cohesion, c (MPa)	50
Internal friction angle, φ (°)	30
Mode I fracture energy, G_{f1} (J/m^2)	20
Mode II fracture energy, G_{f2} (J/m^2)	40
Normal contact penalty, P_n (GPa)	160
Tangential contact penalty, P_s (GPa)	160
Fluid viscosity, μ_f (Pa·s)	1.0×10^{-3}
Fluid density, ρ_f (kg/m^3)	1000
Intrinsic permeability, k (m^2)	1.0×10^{-11}
Biot modulus, M_b (GPa)	22
Porosity, ψ (−)	0.1
Fluid density, ρ_f (kg/m^3)	1000
Initial aperture, a_0 (m)	3.5×10^{-4}
Minimum aperture, a_r (m)	1.0×10^{-5}
Maximum aperture, a_t (m)	9.0×10^{-3}
Fluid exchange coefficient, h_c (m/Pa·s)	5.8×10^{-8}
Solid timestep, Δt_s (s)	2.0×10^{-6}
Fracture seepage timestep, Δt_{ff} (s)	6.0×10^{-9}
Pore seepage timestep, Δt_{fp} (s)	1.0×10^{-7}

original approach. The pore pressure at various steps (5000, 15,000 and 30,000 steps) for the model with $L/h = 100$ is shown in Fig. 16c-d. It can be observed that the pore seepage has reached a steady state after 30,000 steps using the proposed approach, while the fluid flux mainly distributes on the right side of the plate when the original approach is adopted. This also demonstrates the improved computational efficiency of the proposed approach.

5. Application example

To enhance productivity in low permeability reservoirs, the multi-stage hydraulic fracturing technique has been extensively used to generate persistent fractures parallel to the maximum principal *in situ* stress (Yoon et al., 2015). However, the opening of one fracture may cause the deflection of neighboring fractures and suppress their propagation (Duan et al., 2020). Therefore, accurate evaluation of the growing characteristics of multiple hydraulic fractures is crucial for optimizing the design of multi-stage hydraulic fracturing schemes. Here, we establish a homogeneous and isotropic rock model with four injection points to investigate the effect of fluid viscosity on the mechanism of hydraulic fracturing. The width of the rock model is 100 m, and the space between adjacent injection points is 10 m (Fig. 17a). The four injection points are denoted as #1, #2, #3 and #4 from left to right along the horizontal direction. The model consists of 26,904 triangle elements with an average element size of 1.0 m, and the unstructured Delaunay triangulation mesh scheme is employed (Fig. 17b). Prior to fluid injection, the horizontal and vertical *in situ* stresses are applied on the boundaries of rock model and increased gradually from 0 to 10 MPa and 15 MPa, respectively, via a time span of 0.6 s. Then, a constant fluid flow injection rate of $Q = 0.2$ m^2/s is applied at the four injection points. The key input parameters of the rock model are tabulated in Table 9.

Three cases with different fluid viscosities, i.e., $\mu_f = 2 \times 10^{-3}$, 1×10^{-2} and 5×10^{-2} Pa·s, are employed. As shown in Fig. 18a for the first case with $\mu_f = 2 \times 10^{-3}$ Pa·s, the hydraulic fractures are first initiated from injection points #1 and #3, and propagate along the vertical direction ($t = 1.7$ s). As fluid injection continues to $t = 1.85$ s, newly generated fractures occur at injection point #4, and the pressures at injection points 1# and #3 begin to decrease. After that, the fracture lengths at injection points #2 and #4 exceed that at #3, and the fracture propagation at #3 is suppressed ($t = 2.0$ s). In addition, the fluid pressure at #2 does not dissipate along the fracture path. As injection continues to 2.2 s, the fracture length at #2 and #4 is larger than that at #1 and #3, and the maximum fluid pressure mainly distributes in the fracture path at #1. In contrast, for the second case with $\mu_f = 1 \times 10^{-2}$

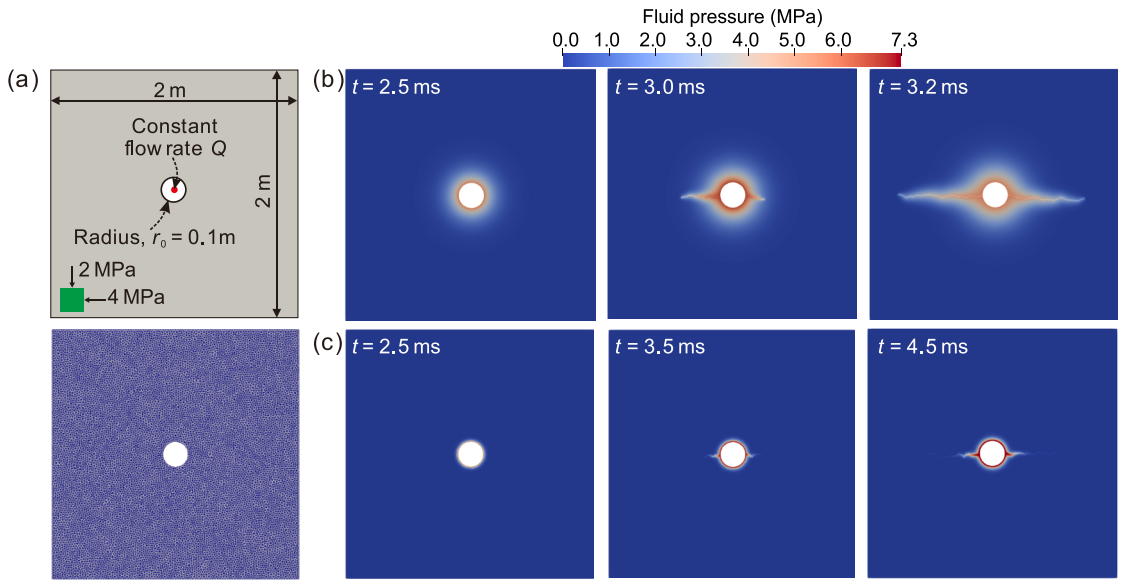

Fig. 15. (a) Model geometry and mesh. Fluid pressure distribution and fracture patterns at different timestamps for scenarios using (b) low and (c) high viscosity fluid.

Table 7
Input parameters in FDEM simulations for hydraulic fracturing in a model with a borehole.

Input parameters	Values
Young's modulus, E (GPa)	55
Bulk density, ρ (kg/m^3)	2600
Poisson's ratio, ν	0.25
Viscous damping coefficient, η (kg/m·s)	1.9×10^5
Tensile strength, f_t (MPa)	4
Cohesion, c (MPa)	30
Internal friction angle, φ (°)	30
Mode I fracture energy, G_{f1} (J/m^2)	10
Mode II fracture energy, G_{f2} (J/m^2)	40
Normal contact penalty, P_n (GPa)	550
Tangential contact penalty, P_s (GPa)	550
Fluid viscosity, μ_f (Pa·s)	1.0×10^{-3}
Fluid density, ρ_f (kg/m^3)	1000
Intrinsic permeability, k (m^2)	1.0×10^{-13}
Biot modulus, M_b (GPa)	11
Porosity, ψ (–)	0.2
Initial aperture, a_0 (m)	1.0×10^{-4}
Minimum aperture, a_r (m)	1.0×10^{-5}
Maximum aperture, a_t (m)	2.0×10^{-3}
Fluid exchange coefficient, h_c (m/Pa·s)	2.5×10^{-8}
Solid timestep, Δt_s (s)	3.0×10^{-7}
Fracture seepage timestep, Δt_{ff} (s)	6.0×10^{-10}
Pore seepage timestep, Δt_{fp} (s)	1.0×10^{-8}

Pa·s shown in Fig. 18b, four hydraulic fractures are initiated with approximately equal length and also propagate along the vertical direction ($t = 1.9$ s). As fluid injection continues to $t = 2.66$ s, the fracture lengths at injection points #1 and #4 are obviously longer than those at #2 and #3, and the fracture propagations at #2 and #3 are inhibited. Furthermore, the injection pressures at #1 and #4 begin to decrease along the fracture paths. As model time evolves to 3.04 s, the fracture propagation at #3 deviates from that at #4. The four hydraulic fractures further propagate to $t = 3.8$ s. For the third case with the highest fluid viscosity $\mu_f = 5 \times 10^{-2}$ Pa·s (Fig. 18c), the four hydraulic fractures are simultaneously initiated from the injection points, and the propagation directions deflect to the two sides of the rock model. Interestingly, the fracture lengths are not dramatically suppressed by each other, and the fracture patterns at #1 and #4 are nearly symmetric with respect to the model center.

The above simulation results demonstrate that high fluid viscosity can weaken the stress shadowing effect and enhance the fracturing efficiency, resulting in roughly equal fracture length at each injection point. Additionally, although the problem specification is symmetric with the same injection rate for each injection point, the fracture propagation at the two inner injection points (i.e., #2 and #3) is more susceptible to the neighboring injection points when low viscosity fluid is injected, thereby leading to unsymmetrical fracture patterns with respect to the model center. The peak pressures at the four injection points when using different fluid viscosities are presented in Fig. 19. It can be seen that for the case using the smallest fluid viscosity (2×10^{-3} Pa·s), fluctuation of peak fluid pressure at the four injection points is encountered due to the interaction between neighboring fractures. The peak fluid pressure at injection point #2 reaches a maximum of ~ 27.8 MPa, probably because the fracture propagation is restricted by fractures at #1 and #3. With the increasing fluid viscosity, the peak fluid pressures at the four injection points are relatively close, which again proves the earlier observations in Fig. 18c that the influence among fractures at neighboring injection points becomes less significant when high viscosity fluid is used.

6. Conclusions

This study proposed a new unified pore-fracture seepage model for simulating the fluid-driven fracturing process in fractured porous media within the FDEM framework. In this proposed hydro-mechanical coupling model, a node binding scheme is adopted to ensure the continuum behavior of pore seepage in rock matrices prior to fracturing onset, which can also achieve the separation of pore pressure nodes by dynamically updating the master–slave list when new fractures are generated. The fracture seepage model that obeys the cubic law is responsible for accurately capturing the fluid flow along fractures.

A series of numerical experiments are conducted to verify the correctness of the proposed hydro-mechanical coupling model. The pore pressure distributions in the thick-wall cylinder and rectangular plate obtained from the FDEM simulations are in good agreement with the analytical solutions, verifying the accuracy of pore seepage simulation of our proposed approach in porous media. In addition, the fracture fluid pressure distribution along the fracture is consistent with the analytical results, which also verifies the accuracy of the fracture seepage model. The simulated fracture aperture in FDEM matches the analytical

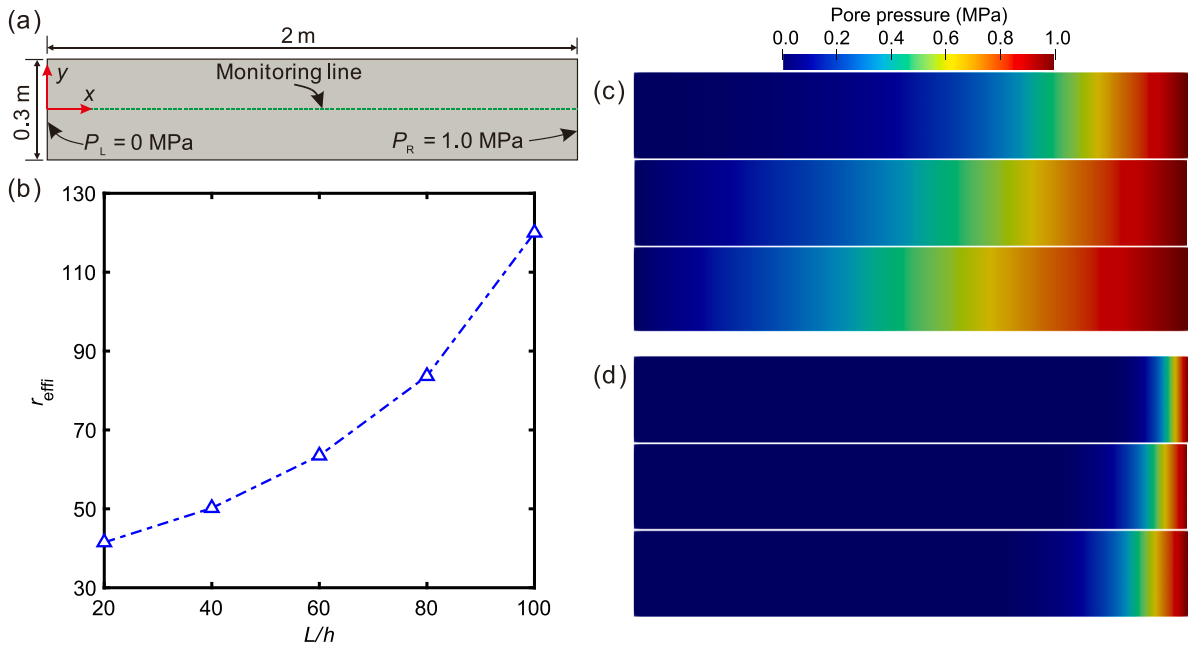

Fig. 16. (a) Model geometry (the monitoring line is marked in green). (b) Comparison of computational efficiency between the proposed and the original approaches with various models. (c) Pore pressure distribution simulated by (c) the proposed and (d) the original approaches at different time steps (5000, 15,000 and 30000) for the model with $L/h = 100$. r_{effi} is a ratio of the computing time needed between the original and proposed approaches upon pore seepage reaching a steady state. L and h denote the width of the plate and average element size, respectively. (For interpretation of the references to colour in this figure legend, the reader is referred to the web version of this article.)

Table 8
Input parameters for the comparison of computational efficiency.

Input parameters	Values
Young's modulus, E (GPa)	30
Bulk density, ρ (kg/m^3)	2700
Poisson's ratio, ν	0.27
Normal contact penalty, P_n (GPa)	300
Tangential contact penalty, P_s (GPa)	300
Fluid viscosity, μ_f (Pa·s)	1.0×10^{-3}
Bulk modulus of the fluid, K_w (GPa)	2.2
Fluid density, ρ_f (kg/m^3)	1000

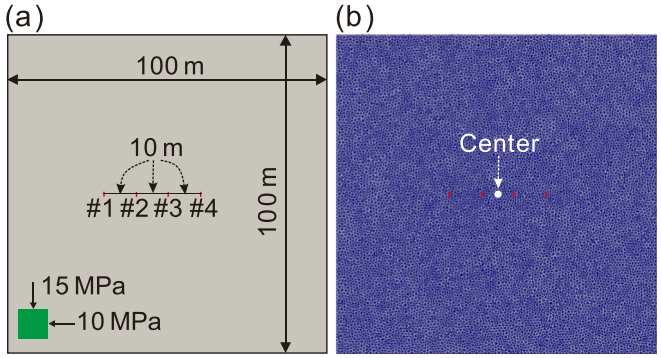

Fig. 17. (a) Model geometry and boundary conditions. (b) Mesh. Four injection points are evenly spaced at 10 m along the horizontal direction, denoted as injection points #1, #2, #3 and #4 from left to right. The center of the specimen is marked by a white dot.

solution, demonstrating the correctness of the proposed hydro-mechanical coupling model. To account for rock fracturing induced by fluid pressure, a square plate containing a single or two pre-existing fractures is employed to demonstrate the capability of the proposed approach in simulating the process of fluid-driven fractures. The resulting fracture paths and failure patterns agree with previous observations. Additionally, the proposed hydro-mechanical model can significantly reduce the computational cost, especially for pore seepage simulation.

Table 9
Input parameters in FDEM simulations for multiple hydraulic fracturing.

Input parameters	Values
Young's modulus, E (GPa)	40
Bulk density, ρ (kg/m^3)	2400
Poisson's ratio, ν	0.22
Viscous damping coefficient, η (kg/m·s)	8.1×10^6
Tensile strength, f_t (MPa)	5
Cohesion, c (MPa)	25
Internal friction angle, φ (°)	30
Mode I fracture energy, G_{f1} (J/m^2)	30
Mode II fracture energy, G_{f2} (J/m^2)	60
Normal contact penalty, P_n (GPa)	400
Tangential contact penalty, P_s (GPa)	400
Fluid density, ρ_f (kg/m^3)	1000
Intrinsic permeability, k (m^2)	3.0×10^{-13}
Biot modulus, M_b (GPa)	11
Porosity, ψ (−)	0.2
Initial aperture, a_0 (m)	7.0×10^{-5}
Minimum aperture, a_r (m)	1.0×10^{-5}
Maximum aperture, a_t (m)	7.0×10^{-3}
Fluid exchange coefficient, h_c (m/Pa·s)	8.1×10^{-7}
Solid timestep, Δt_s (s)	1.0×10^{-5}
Fracture seepage timestep, Δt_{ff} (s)	4.0×10^{-9}
Pore seepage timestep, Δt_{fp} (s)	9.0×10^{-5}

Following this, one application example is performed to preliminarily test the effect of fluid viscosity on the propagation of multiple hydraulic fractures and further verify the robustness of the proposed hydro-mechanical coupling approach. The numerical results reveal that the high fluid viscosity can weaken the stress shadowing effect and enhance the fracturing efficiency. The proposed unified pore-fracture seepage model may help enhance FDEM's applicability for estimating the propagation process of hydraulic fracturing associated with

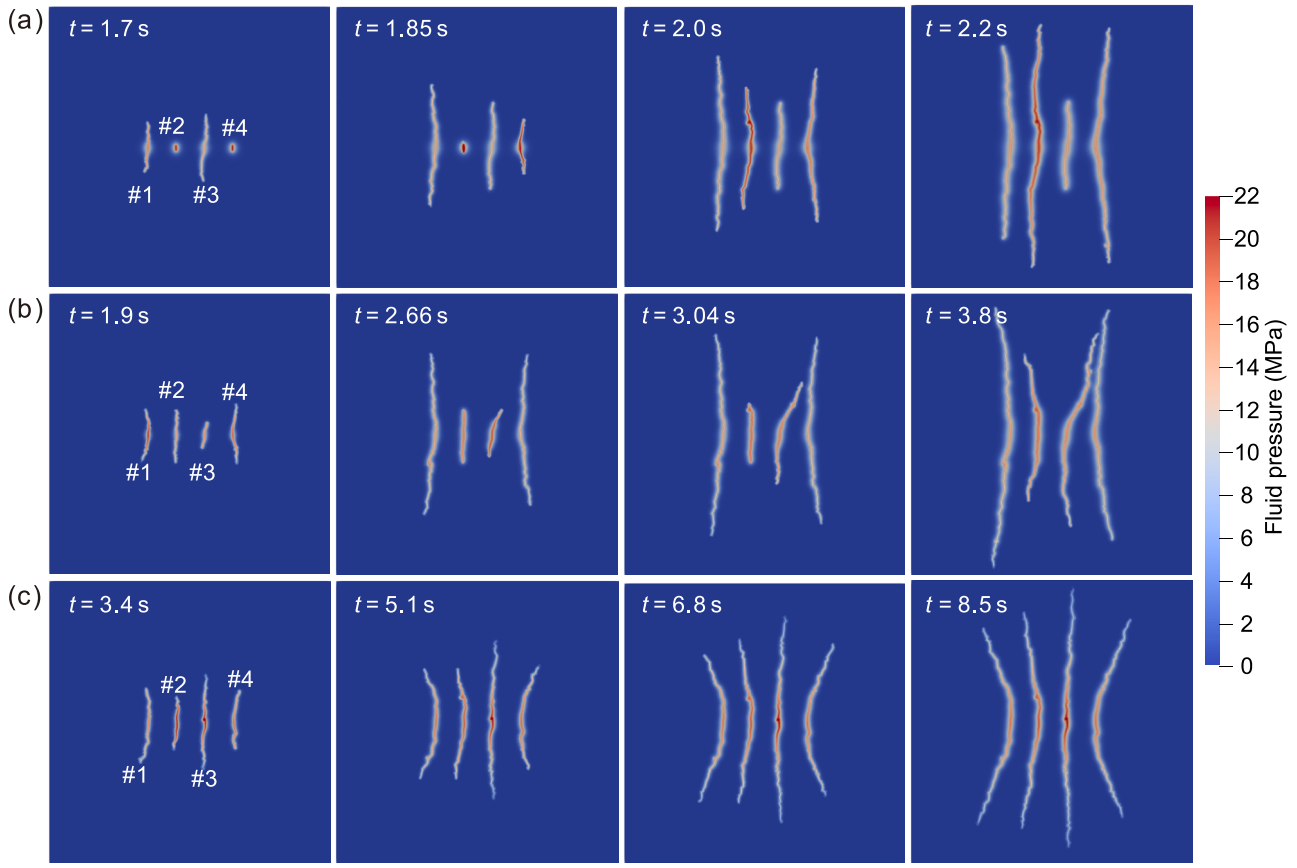

Fig. 18. Fluid pressure distribution associated with hydraulic fracture propagation for the three cases using different fluid viscosities: (a) 2×10^{-3} Pa·s, (b) 1.0×10^{-2} Pa·s and (c) 5×10^{-2} Pa·s.

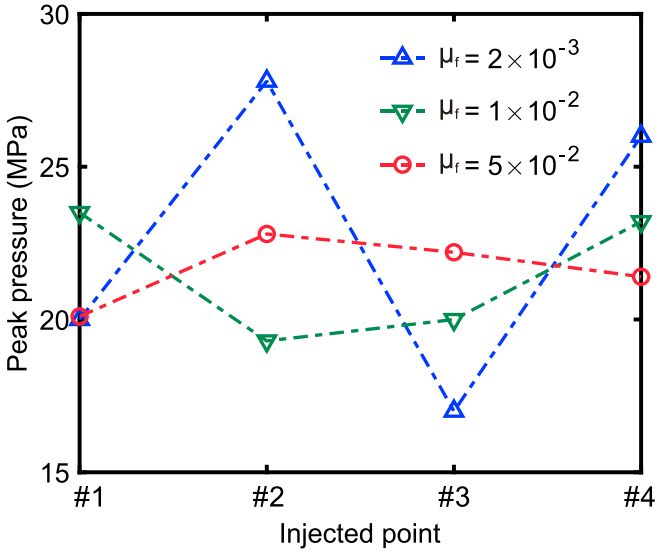

Fig. 19. Peak pressures at the four injection points for the three cases using different fluid viscosities.

unconventional energy exploitation (e.g., shale and hot dry rock). Extension of the unified pore-fracture seepage model to 3D will be reported in the near future.

Author contributions

The authors confirm contributions to the paper as below: Research design: Ke Gao; Analysis of numerical results: Weibing Cai, Yan Qiao and Shu-Gang Ai; Draft manuscript preparation: Weibing Cai; Revised manuscript and funding support: Ke Gao and Yu Feng. All authors have reviewed the results and approved the final version of the manuscript.

CRediT authorship contribution statement

Weibing Cai: Writing – original draft, Software, Methodology, Formal analysis. **Ke Gao:** Writing – review & editing, Supervision, Funding acquisition. **Yan Qiao:** Validation. **Shu-Gang Ai:** Validation, Data curation. **Yu Feng:** Writing – original draft.

Declaration of competing interest

The authors declare that they have no known competing financial interests or personal relationships that could have appeared to influence the work reported in this paper.

Data availability

Data will be made available on request.

Acknowledgments

This work is supported by the Shenzhen Science and Technology Program (JCYJ20220530113612028), the Guangdong Basic and Applied Basic Research Foundation (2023A1515011244), and the Guangdong Provincial Key Laboratory of Geophysical High-resolution Imaging Technology (2022B1212010002).

References

Barenblatt, G.I., Zheltov, I.P., Kochina, I.N., 1960. Basic concepts in the theory of seepage of homogeneous liquids in fissured rocks. J. Appl. Math. Mech. 24 (5), 1286–1303.

Belytschko, T., Lu, Y.Y., Gu, L., 1994. Element-free Galerkin methods. Int. J. Numer. Methods Eng. 37 (2), 229–256.

Berkowitz, B., 2002. Characterizing flow and transport in fractured geological media: A review. Adv. Water Resour. 25 (8), 861–884.

Board, M., 1989. UDEC (Universal Distinct Element Code) Version ICG1. 5. Nuclear Regulatory Commission, Washington, DC (USA).

Cai, W., Li, Y., Wang, K., 2022. Crack propagation mechanism of rock-like specimens containing non-parallel flaws subjected to internal hydraulic pressure and shear loading. Theor. Appl. Fract. Mech. 119, 103350.

Cai, W., Gao, K., Ai, S., Wang, M., Feng, Y.T., 2023. Implementation of extrinsic cohesive zone model (ECZM) in 2D finite-discrete element method (FDEM) using node binding scheme. Comput. Geotech. 159, 105470.

Carlslaw, H., Jaeger, J., 1959. Conduction of Heat in Solids. Oxford University Press, America.

Crank, J., 1975. The mathematics of diffusion. Oxford University Press, Oxford, UK.

Cundall, P.A., Strack, O.D.L., 1979. A discrete numerical model for granular assemblies. Geotechnique. 29 (1), 47–65.

Duan, K., Li, Y., Yang, W., 2020. Discrete element method simulation of the growth and efficiency of multiple hydraulic fractures simultaneously-induced from two horizontal wells. Geomech. Geophys. Geo-Energy Geo-Resour. 7 (1), 3.

Duan, K., Li, X., Kwok, C.-Y., Zhang, Q., Wang, L., 2021. Modeling the orientation- and stress-dependent permeability of anisotropic rock with particle-based discrete element method. Int. J. Rock Mech. Min. Sci. 147, 104884.

Duarte, C.A., Hamzeh, O.N., Liszka, T.J., Tworzydlo, W.W., 2001. A generalized finite element method for the simulation of three-dimensional dynamic crack propagation. Comput. Meth. Appl. Mech. Eng. 190 (15), 2227–2262.

Euser, B., Rougier, E., Lei, Z., Knight, E.E., Frash, L.P., Carey, J.W., Viswanathan, H., Munjiza, A., 2019. Simulation of fracture coalescence in granite via the combined finite-discrete element method. Rock Mech. Rock Eng. 52 (9), 3213–3227.

Fjær, E., Holt, R., Horsrud, P., Fjaer, E., Raaen, A., Risnes, R., Fjar, E., 2008. Petroleum Related Rock Mechanics. Elsevier.

Fukuda, D., Mohammadnejad, M., Liu, H., Dehkhoda, S., Chan, A., Cho, S.H., Min, G.J., Han, H., Kodama, J.I., Fujii, Y., 2019a. Development of a GPGPU-parallelized hybrid finite-discrete element method for modeling rock fracture. Int. J. Numer. Anal. Methods Geomech. 43 (10), 1797–1824.

Fukuda, D., Mohammadnejad, M., Liu, H., Zhang, Q., Zhao, J., Dehkhoda, S., Chan, A., Kodama, J.-I., Fujii, Y., 2019b. Development of a 3D Hybrid Finite-Discrete Element Simulator Based on GPGPU-Parallelized Computation for Modelling Rock Fracturing Under Quasi-Static and Dynamic Loading Conditions. Rock Mech. Rock Eng. 53 (3), 1079–1112.

Fukuda, D., Nihei, E., Cho, S.-H., Oh, S., Nara, Y., Kodama, J.-I., Fujii, Y., 2020. Development of a numerical simulator for 3-D dynamic fracture process analysis of rocks based on hybrid FEM-DEM using extrinsic cohesive zone model. Mater. Trans. 61 (9), 1767–1774.

Fukuda, D., Liu, H., Zhang, Q., Zhao, J., Kodama, J.-I., Fujii, Y., Chan, A.H.C., 2021. Modelling of dynamic rock fracture process using the finite-discrete element method with a novel and efficient contact activation scheme. Int. J. Rock Mech. Min. Sci. 138, 104645.

Gläser, D., Helmig, R., Flemisch, B., Class, H., 2017. A discrete fracture model for two-phase flow in fractured porous media. Adv. Water Resour. 110, 335–348.

Han, H., Fukuda, D., Liu, H., Salmi, E.F., Sellers, E., Liu, T., Chan, A., 2020. Combined finite-discrete element modelling of rock fracture and fragmentation induced by contour blasting during tunnelling with high horizontal in-situ stress. Int. J. Rock Mech. Min. Sci. 127, 104214.

He, R., Rong, G., Tan, J., Phoon, K.-K., Quan, J., 2022. Numerical evaluation of heat extraction performance in enhanced geothermal system considering rough-walled fractures. Renew. Energy. 188, 524–544.

Itasca, 2005. FLAC User's guide. Itasca Consulting Group Inc, Minnesota.

Jing, L., Hudson, J.A., 2002. Numerical methods in rock mechanics. Int. J. Rock Mech. Min. Sci. 39 (4), 409–427.

Joulin, C., Xiang, J., Latham, J.-P., 2020. A novel thermo-mechanical coupling approach for thermal fracturing of rocks in the three-dimensional FDEM. Comput. Part. Mech. 7 (5), 935–946.

Khoei, A.R., Mortazavi, S.M.S., 2020. Thermo-hydro-mechanical modeling of fracturing porous media with two-phase fluid flow using X-FEM technique. Int. J. Numer. Anal. Methods Geomech. 44 (18), 2430–2472.

Khoei, A.R., Vahab, M., Hirmand, M., 2018. An enriched–FEM technique for numerical simulation of interacting discontinuities in naturally fractured porous media. Comput. Meth. Appl. Mech. Eng. 331, 197–231.

Knight, E.E., Rougier, E., Lei, Z., Euser, B., Chau, V., Boyce, S.H., Gao, K., Okubo, K., Froment, M., 2020. HOSS: an implementation of the combined finite-discrete element method. Comput. Part. Mech. 7, 765–787.

Lamb, A.R., Gorman, G.J., Elsworth, D., 2013. A fracture mapping and extended finite element scheme for coupled deformation and fluid flow in fractured porous media. Int. J. Numer. Anal. Methods Geomech. 37 (17), 2916–2936.

Lewis, R.W., Schrefler, B.A., 1998. The Finite Element Method in the Static and Dynamic Deformation and Consolidation of Porous Media. Wiley, Chichester.

Lisjak, A., Kaifosh, P., He, L., Tatone, B.S.A., Mahabadi, O.K., Grasselli, G., 2017. A 2D, fully-coupled, hydro-mechanical, FDEM formulation for modelling fracturing processes in discontinuous, porous rock masses. Comput. Geotech. 81, 1–18.

Liu, D., Shen, Z., Xu, L., Gan, L., Li, G., 2018. Experimental study on critical internal water pressure of hydraulic fracturing of fractured rock mass. South North Water Transf Water Sci Technol. 16 (02), 140–145.

Lobao, M.C., 2007. Finite element modelling of hydraulic fracture flow in porous media. Swansea University (United Kingdom).

Ma, P., 2022. Study on damage and seepage characteristics of fractured rock mass by peridynamic method. Shandong University.

Maeda, Y., Ogata, S., Fukuda, D., Liu, H., Inui, T., 2024. Development of a GPGPU-parallelized FDEM based on extrinsic cohesive zone model with master-slave algorithm. Comput. Geotech. 166, 105942.

Mohammadnejad, T., Khoei, A.R., 2013. An extended finite element method for hydraulic fracture propagation in deformable porous media with the cohesive crack model. Finite Elem. Anal. Des. 73, 77–95.

Mosharaf-Dehkordi, M., 2022. A fixed point multi-scale finite volume method: Application to two-phase incompressible fluid flow through highly heterogeneous porous media. J. Comput. Phys. 462, 111219.

Munjiza, A., 1992. Discrete elements in transient dynamics of fractured media. Swansea University.

Munjiza, A., 2004. The combined finite-discrete element method. Wiley, London.

Munjiza, A., Andrews, K.R.F., 1998. NBS contact detection algorithm for bodies of similar size. Int. J. Numer. Methods Eng. 43 (1), 131–149.

Munjiza, A., Knight, E.E., Rougier, E., 2011. Computational Mechanics of Discontinua. Willey, London.

Nagel, N.B., Sanchez-Nagel, M.A., Zhang, F., Garcia, X., Lee, B., 2013. Coupled Numerical Evaluations of the Geomechanical Interactions Between a Hydraulic Fracture Stimulation and a Natural Fracture System in Shale Formations. Rock Mech. Rock Eng. 46 (3), 581–609.

Ni, T., Pesavento, F., Zaccariotto, M., Galvanetto, U., Schrefler, B.A., 2021. Numerical simulation of forerunning fracture in saturated porous solids with hybrid FEM/Peridynamic model. Comput. Geotech. 133, 104024.

Papoulia, K.D., Sam, C.-H., Vavasis, S.A., 2003. Time continuity in cohesive finite element modeling. Int. J. Numer. Methods Eng. 58 (5), 679–701.

Paul, B., Faivre, M., Massin, P., Giot, R., Colombo, D., Golfier, F., Martin, A., 2018. 3D coupled HM–XFEM modeling with cohesive zone model and applications to non planar hydraulic fracture propagation and multiple hydraulic fractures interference. Comput. Meth. Appl. Mech. Eng. 342, 321–353.

Profit, M., Dutko, M., Yu, J., Cole, S., Angus, D., Baird, A., 2016. Complementary hydro-mechanical coupled finite/discrete element and microseismic modelling to predict hydraulic fracture propagation in tight shale reservoirs. Comput. Part. Mech. 3 (2), 229–248.

Qin, M., Yang, D., Chen, W., Xia, X., 2021. Hydraulic fracturing network modeling based on peridynamics. Eng. Fract. Mech. 247, 107676.

Réthoré, J., Borst, R.d., Abellan, M.-A., 2007. A two-scale approach for fluid flow in fractured porous media. Int. J. Numer. Methods Eng. 71 (7), 780–800.

Sam, C.-H., Papoulia, K.D., Vavasis, S.A., 2005. Obtaining initially rigid cohesive finite element models that are temporally convergent. Eng. Fract. Mech. 72 (14), 2247–2267.

Schwartzkopff, A.K., Sainoki, A., Elsworth, D., 2021. Numerical simulation of mixed aseismic/seismic fault-slip induced by fluid injection using coupled X-FEM analysis. Int. J. Rock Mech. Min. Sci. 147, 104871.

Shi, G.H., Goodman, R.E., 1985. Two dimensional discontinuous deformation analysis. Int. J. Numer. Anal. Methods Geomech. 9 (6), 541–556.

Sun, H., Xiong, F., Wu, Z., Ji, J., Fan, L., 2022. An extended numerical manifold method for two-phase seepage–stress coupling process modelling in fractured porous medium. Comput. Meth. Appl. Mech. Eng. 391, 114514.

Tatone, B.S.A., Grasselli, G., 2015. A calibration procedure for two-dimensional laboratory-scale hybrid finite–discrete element simulations. Int. J. Rock Mech. Min. Sci. 75, 56–72.

Ulloa, J., Noii, N., Alessi, R., Aldakheel, F., Degrande, G., François, S., 2022. Variational modeling of hydromechanical fracture in saturated porous media: A micromechanics-based phase-field approach. Comput. Meth. Appl. Mech. Eng. 396, 115084.

Vahab, M., Khoei, A.R., Khalili, N., 2019. An X-FEM technique in modeling hydro-fracture interaction with naturally-cemented faults. Eng. Fract. Mech. 212, 269–290.

van Opstal, T.M., van Brummelen, E.H., 2013. A finite-element/boundary-element method for large-displacement fluid–structure interaction with potential flow. Comput. Meth. Appl. Mech. Eng. 266, 57–69.

Wang, Z., Liu, Q., Wang, Y., 2021. Thermo-mechanical FDEM model for thermal cracking of rock and granular materials. Powder Technol. 393, 807–823.

Wu, Z., Cui, W., Weng, L., Liu, Q., 2022. A 2D FDEM-based THM coupling scheme for modeling deformation and fracturing of the rock mass under THM effects. Comput. Geotech. 152, 105019.

Wu, D., Li, H., Shao, Z., Chen, S., Zhou, C., Liu, L., 2021. Effects of infilling materials on mechanical behaviors and cracking process of pre-cracked rock: Insights from a hybrid continuum-discontinuum method. Eng. Fract. Mech. 253, 107843.

Xing, J., Zhao, C., 2023. A hydro-mechanical phase field model for hydraulically induced fractures in poroelastic media. Comput. Geotech. 159, 105418.

Yan, C., Jiao, Y.-Y., 2018. A 2D fully coupled hydro-mechanical finite-discrete element model with real pore seepage for simulating the deformation and fracture of porous medium driven by fluid. Comput. Struct. 196, 311–326.

Yan, C., Jiao, Y.-Y., Yang, S., 2018. A 2D coupled hydro-thermal model for the combined finite-discrete element method. Acta Geotech. 14 (2), 403–416.

Yan, C., Fan, H., Huang, D., Wang, G., 2021. A 2D mixed fracture–pore seepage model and hydromechanical coupling for fractured porous media. Acta Geotech. 16, 3061–3086.

Yan, C., Guo, H., Tang, Z., 2022a. Three-dimensional continuous-discrete pore-fracture mixed seepage model and hydro-mechanical coupling model to simulate hydraulic fracturing. Geoenergy Sci. Eng. 215, 110510.
Yan, C., Zheng, H., 2016. A two-dimensional coupled hydro-mechanical finite-discrete model considering porous media flow for simulating hydraulic fracturing. Int. J. Rock Mech. Min. Sci. 88, 115–128.
Yan, C., Xie, X., Ren, Y., Ke, W., Wang, G., 2022b. A FDEM-based 2D coupled thermal-hydro-mechanical model for multiphysical simulation of rock fracturing. Int. J. Rock Mech. Min. Sci. 149, 104964.
Yan, C., Wang, Y., Xie, X., Ali, S., Sheng, Z., 2023. A 2D continuous-discrete mixed seepage model considering the fluid exchange and the pore pressure discontinuity across the fracture for simulating fluid-driven fracturing. Acta Geotech. 18, 5791–5810.
Yang, L., Wu, S., Gao, K., Shen, L., 2022. Simultaneous propagation of hydraulic fractures from multiple perforation clusters in layered tight reservoirs: Non-planar three-dimensional modelling. Energy. 254, 124483.
Yoon, J.S., Zimmermann, G., Zang, A., 2015. Numerical investigation on stress shadowing in fluid injection-induced fracture propagation in naturally fractured geothermal reservoirs. Rock Mech. Rock Eng. 48, 1439–1454.
Yu, S., Ren, X., Zhang, J., Wang, H., Sun, Z., 2021. An Improved Smoothed Particle Hydrodynamics Method and Its Application in Rock Hydraulic Fracture Modelling. Rock Mech. Rock Eng. 54 (12), 6039–6055.